Originally published as:

Erosion of the Rwenzori Mountains, East African Rift, from in situ-produced cosmogenic [10]Be

S. Roller,[1,2] H. Wittmann,[3] M. Kastowski,[1] and M. Hinderer[1]

[1] High relief and steep topography are thought to result in high erosion rates. In the Rwenzori Mountains of the Albert Rift, East Africa, where more than 3 km of relief have formed during uplift of the Rwenzori fault block, overall low denudation rates prevail. We measured in situ-derived cosmogenic denudation rates of 28.2 to 131 mm/kyr in mountainous catchments, and rates of 7.8 to 17.7 mm/kyr on the adjacent low-relief East African Plateau. These rates are roughly an order of magnitude lower than in other settings of similar relief. We present an extensive geomorphological analysis, and find that denudation rates are positively correlated with relief, hillslope gradient, and channel steepness, indicating that river incision controls erosional processes. In most upper headwater reaches above Quaternary ELA levels (>4500 m a.s.l.), glacial imprinting, inherited from several older and recent minor glaciation stages, prevails. In regions below 4500 m a.s.l., however, mild climatic conditions impede frost shattering, favor dense vegetation, and minimize bare rock areas and associated mass wasting. We conclude that erosion of the Rwenzori Mountains is significantly slower than corresponding rates in other mountains of high relief, due to a combination of factors: extremely dense mountain cloud forest vegetation, high rock strength of gneiss and amphibolite lithologies, and low internal fracturing due to the extensional tectonic setting. This specific combination, unique to this extensional tropical setting, leads to unexpected low erosion rates that cannot outpace post-Pliocene ongoing rock uplift of the Rwenzori fault block.

1. Introduction

[2] Important advances in deciphering the coupling of climate, tectonics, and erosion in mountain building have been achieved recently using in situ-produced cosmogenic nuclides to derive basin-wide, millennial-scale denudation rates [*Matmon et al.*, 2003; *Wobus et al.*, 2005; *Wittmann et al.*, 2007; *Ouimet et al.*, 2009]. Work in recent decades has provided rates across the globe and across a range of tectonic, climatic, and geomorphic settings [see *Portenga and Bierman*, 2011]. However, for low-latitude settings with their tropical humid conditions, very few studies using terrestrial cosmogenic nuclides (TCN) are available [e.g., *Hewawasam*

et al., 2003; *Vanacker et al.*, 2007]. Such settings represent an important end-member climate for considering the role of vegetation in controlling the physical and chemical processes of denudation. Moreover, existing erosion data from cosmogenic nuclides in extensional settings are limited to high-latitude settings [e.g., *Granger et al.*, 1996; *Riebe et al.*, 2000], where the function of a tropical climate with extensive vegetation and soil cover in regulating erosion cannot be studied. Thus, our understanding of the tectonic and climatic controls on erosion is incomplete and the data presented here are a significant contribution to the currently existing global TCN-derived denudation rate database [*Portenga and Bierman*, 2011].

[3] The specific setting of the Rwenzori Mountains (Uganda), comprising a rapidly uplifting fault block in the southern Albert rift segment (see Figure 1) presents interesting boundary conditions that allow us to study the interactions of climate and tectonics: a so-called "mountain cloud forest" climate, featuring high precipitation with lack of seasonality, dense vegetation, and soil cover up to the highest peaks (see Figure 2). Unusually, these climatic characteristics are combined with steep relief, a rugged, glacially sculpted topography and high absolute altitudes, but overall minor rock deformation of Precambrian metamorphic basement rocks in an extensional tectonic regime. The aim of this

[1]Institut für Angewandte Geowissenschaften, Technische Universität Darmstadt, Darmstadt, Germany.
[2]Now at Senckenberg Forschungsinstitut, Frankfurt am Main, Germany.
[3]Sektion Oberflächennahe Geochemie, Helmholtz Zentrum Potsdam, Deutsches GeoForschungsZentrum, Potsdam, Germany.

Corresponding author: S. Roller, Senckenberg Forschungsinstitut, Senckenberganlage 25, D-60235 Frankfurt am Main, Germany. (sybille.roller@senckenberg.de)
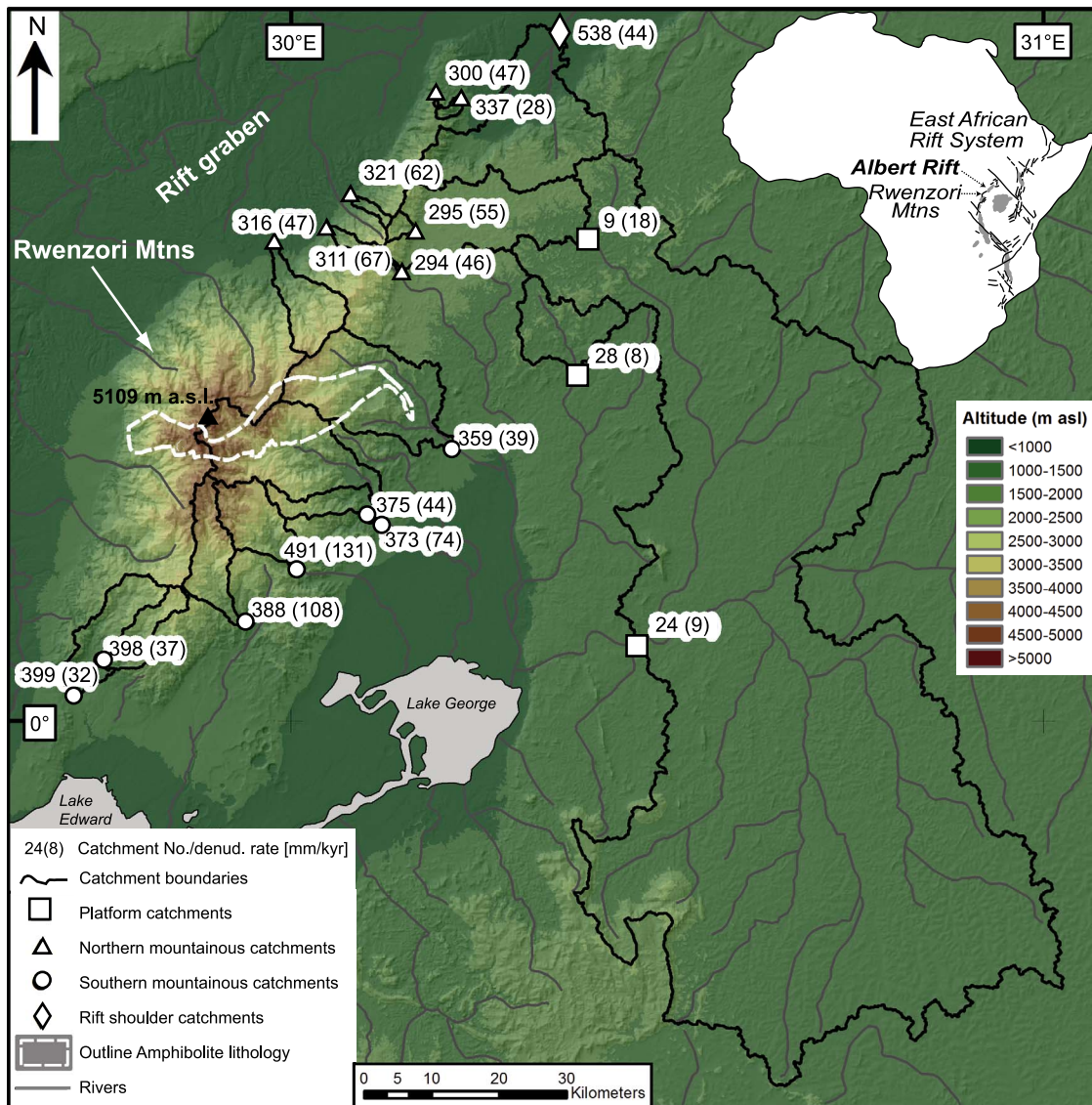
Figure 1. Overview of the Rwenzori Mountains and adjacent Albert Rift in their equatorial position in the northern part of the Western Rift branch (small overview map). Large map derived from ASTER 30 m DEM, with sampled basins marked in black and river drainage pattern in gray. The outline of quartz-free amphibolitic lithology is marked on the SE mountain flank (white dashed line). The sampled basins are divided into 4 groups: squares = rift shoulder platform, triangles = northern range of Rwenzori block, circles = southern Rwenzori block, rhombohedra = rift shoulder. Given numbers indicate basin number, with numbers in brackets indicating the denudation rate in mm/kyr. Denudation rates of basins 373, 388, and 491 may be overestimates due to glaciations effects (see Section 5.2.1).

study is to examine the couplings of these factors within the frame of the large interdisciplinary RIFTLINK project (www.riftlink.de). The RIFTLINK project focuses on collecting basic data in the fields of geology, geophysics, geochemistry, palaeontology, etc., specifically for the low-latitude setting of the Rwenzori Mountains located in the Ugandan part of the East African Rift System. In the context of this project, we present a new data set of in situ ^{10}Be-derived basin-wide denudation rates (Table 1) that decipher the Holocene erosional evolution of this mountain belt and reflect a combination of controlling factors unique to tropical extensional settings.

2. Geological Background and Study Area

2.1. Overall and Tectonic Setting

[4] Since the Miocene, the western branch of the East African Rift System (EARS) (see small insert map in Figure 1) has evolved to its recent structure - a slightly convex alignment of mature rift graben segments [*Chorowicz*, 2005;
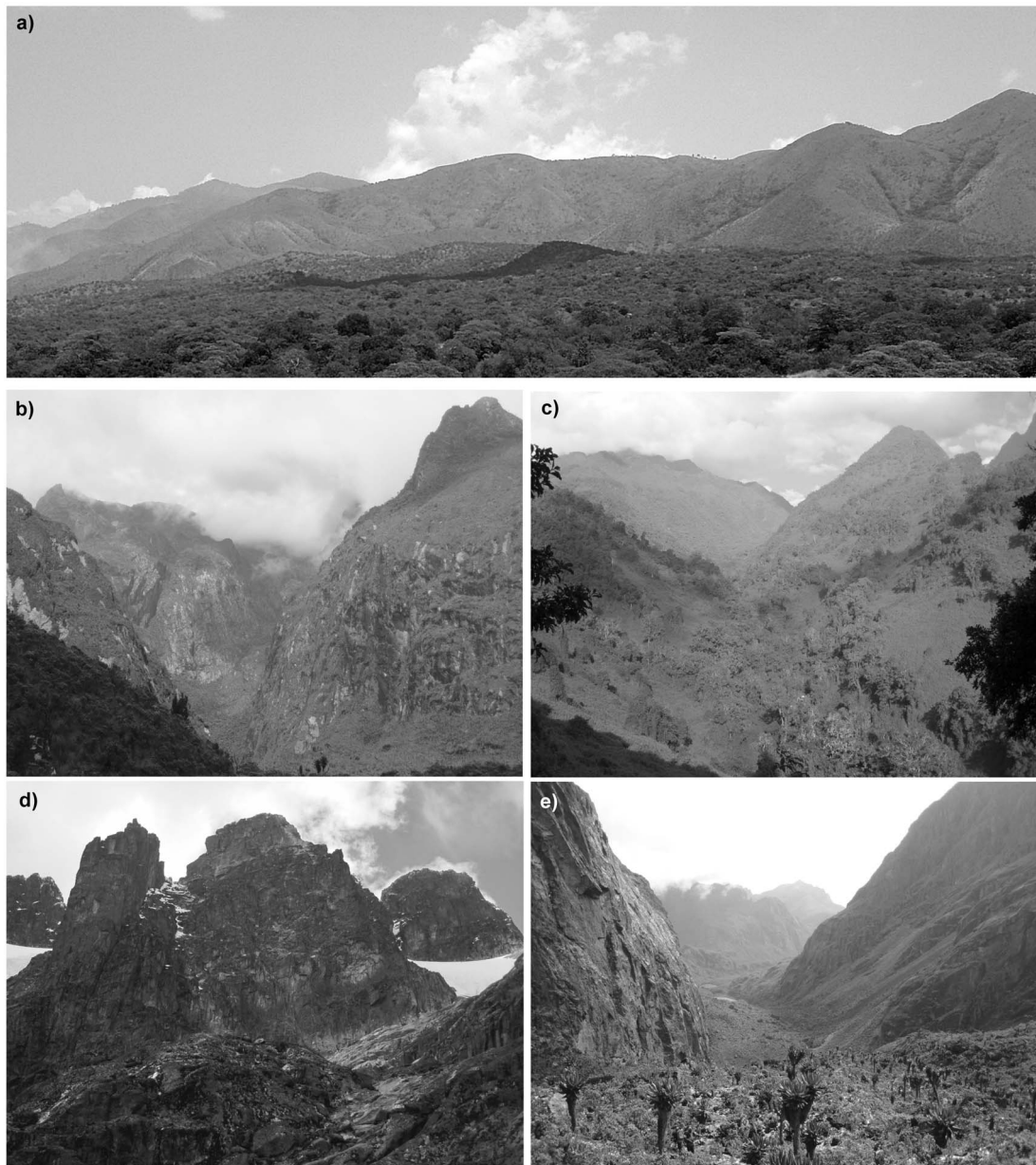
Figure 2. Representative photographs of the typical Rwenzori Mountain landscape of the investigated eastern flank. (a) View toward SW from Albert rift graben to the northern Rwenzori Mountain range, maximum elevation of the ridge is ~2500 m a.s.l., (b) view from 3780 m a.s.l. altitude along the main valley of Mubuku catchment (373) toward N into narrow U-shaped tributary valley of Mubuku river (peaks at ~4500 m a.s.l.), (c) view down the main valley of catchment 373 toward W into broad lower Mubuku valley (2650 m a.s.l); moraine covered hillslopes are densely vegetated by montane forest, (d) view of the rugged bare rock peak region of the Rwenzori Mountains (max. 5109 m a.s.l.) which is covered by (e) today's glacier view from upper Mubuku catchment toward southeast into a glacier-cut valley which leads to moraine-dammed lakes. Moraines are from Omirubaho stage (11.6 kyr) [*Kaser and Osmaston*, 2002]; in the foreground: moraine material covered by afroalpine belt-type vegetation.

Ebinger, 1989; *Bauer et al.*, 2010]. In its northernmost part, the Western Rift shows two roughly N-S oriented lake-filled rift segments, the Edward and Albert Rifts, which are propagating toward each other [*Koehn et al.*, 2007]. The Rwenzori block is located in the intersection of the two rift segments (Figure 1) [*Koehn et al.*, 2007] and is bounded by a series of high offset normal faults [*Ebinger*, 1989;

Chorowicz, 2005]. Over its length of ca. 20 km, the northern range of the fault block is currently detaching from the eastern graben shoulder, whereas in the south it is already fully detached [*Koehn et al.*, 2007].

[5] The narrow and elongated northern range of the Rwenzori Mountains reaches altitudes between 2000 and 3500 m above sea level (m a.s.l.). The southern part of the

Table 1. Cosmogenic Nuclide Analytical and Derived Denudation Rate Data

River	Sample[a]	Grain Size (mm)	Sample Weight (g)	^{10}Be Concentration[b] ($\times10^4$ at/g$_{(Qz)}$)	Total Production Rate[c] (at/g$_{(Qz)}$/yr)	Shielding Factor[d]	Corr. Spallogenic Production Rate[e] (at/g$_{(Qz)}$/yr)	Corr. Total Muonic Production Rate[e] (at/g$_{(Qz)}$/yr)	Denudation Rate[f] (mm/kyr)	Internal Uncertainty[g] (mm/kyr)	External Uncertainty[h] (mm/kyr)	Apparent Age[i] (kyr)
Northern Mountainous Catchments												
Mahoma	294	0.5–1.0	30.90	17.73 ± 0.89	11.63	0.87	9.82	0.29	45.5	2.4	5.8	17.6
Dunga	295–1	0.5–1.0	32.84	15.93 ± 0.46	12.32	0.91	10.89	0.31	56.0	1.6	6.8	14.3
Dunga	295–2	0.5–1.0	25.05	16.84 ± 0.84	"	"	"	"	52.9	2.7	6.8	15.1
Sempaya	300	0.5–1.0	25.97	13.58 ± 0.40	7.89	0.94	7.17	0.26	46.6	1.4	5.6	18.4
Rugo	311a	0.5–1.0	31.78	13.09 ± 0.47	12.89	0.89	11.21	0.31	70.0	2.5	8.6	11.4
Rugo	311b	1.0–1.25	25.27	14.28 ± 0.42	"	"	"	"	64.0	1.9	7.5	12.4
Rutoba	316	0.5–1.0	11.20	22.33 ± 0.68	14.90	0.92	13.37	0.34	47.3	1.5	5.9	16.4
Humiya	321	0.5–1.0	30.69	11.81 ± 0.35	9.57	0.92	8.52	0.28	61.8	1.8	7.5	13.5
Itojo	337	0.5–1.0	24.47	19.61 ± 0.57	6.91	0.94	6.25	0.25	28.2	0.8	3.3	30.4
Southern Mountainous Catchments												
Ruimi	359	1.0–1.25	19.95	23.48 ± 0.68	12.12	0.95	11.20	0.32	38.6	1.1	4.8	20.5
Mubuku	373–1[j]	0.5–1.0	34.12	18.89 ± 0.54	20.50	0.92	18.42	0.39	74.7	2.2	9.0	10.1
Mubuku	373–2[j]	0.5–1.0	25.78	19.3 ± 1.1	"	"	"	"	72.9	4.3	9.7	10.3
Isebo	375	0.5–1.0	29.70	20.67 ± 0.51	12.08	0.94	11.07	0.31	43.5	1.1	5.2	18.2
Nyamagasani	388a[j]	0.5–1.0	34.51	13.13 ± 0.30	21.90	0.90	19.33	0.40	112.7	2.7	13.3	6.7
Nyamagasani	388b[j]	1.0–1.25	26.66	14.36 ± 0.43	"	"	"	"	103.0	3.1	12.3	7.3
upper Lubilia	398	0.5–1.0	27.22	23.81 ± 0.69	11.68	0.96	10.87	0.32	37.2	1.1	4.5	21.4
Lubilia	399	1.0–1.25	32.01	21.98 ± 0.63	9.11	0.95	8.41	0.28	32.3	0.9	4.0	25.4
Nyamwamba	491[j]	0.5–1.0	10.11	10.5 ± 1.2	20.59	0.89	17.84	0.38	131.0	14.7	21.2	5.8
Platform Catchments												
northern Mpanga	9	0.5–1.0	66.29	37.32 ± 0.36	8.39	0.99	7.99	0.28	17.7	0.2	2.1	45.6
southern Mpanga	28	0.5–1.0	52.55	70.36 ± 0.60	7.49	1.00	7.20	0.27	7.8	0.1	0.9	99.8
Dura	24	0.5–1.0	57.73	62.34 ± 0.96	7.24	1.00	6.95	0.27	9.2	0.1	1.1	85.1
Rift Shoulder Catchment												
Wasa	538	0.5–1.0	60.11	12.68 ± 0.29	6.47	0.98	6.07	0.25	43.9	1.0	5.1	20.2

[a]All samples have been measured at SUERC, except 295–2 and 373–2, which were measured at ETH and denote lab replicates; "a" and "b" denote different grain size fractions.
[b]Corrected for blank, with combined analytical and blank error; an average blank ^{10}Be/^{9}Be ratio is $4.5 \pm 1.6 \times 10^{-15}$.
[c]Total production rate, calculated for fast and slow muonic and high-energy neutrons using *Balco et al.*'s [2008] dataset (see text) and the scaling scheme of *Dunai* [2000].
[d]Shielding factor including topography, shielding due to ice and snow, and different Qz-contents.
[e]Spallogenic and total muonic (including contributions from negative and fast muons) production rate, corrected using given shielding factor.
[f]Denudation rate calculated with a rock density of 2.7 g/cm^3.
[g]1 sigma error on ^{10}Be measurement and blank (internal error for inter-sample comparison).
[h]Total 1 sigma external error gives combined error on ^{10}Be measurement and blank correction. Included is also a 10% production rate error due to topographic and snow/ice shielding, scaling, and variations in Earth's geomagnetic field (the latter has not been corrected for, see text for details).
[i]Gives time spent in upper ~60 cm of eroding layer.
[j]Denudation rates for these basins may be biased by non-steady denudation due to recent glaciation and thus may overestimate true erosion (see text for details).

fault block reaches altitudes of up to 5109 m a.s.l., with a mean relief calculated for all southern catchments of ~2800 m (we define relief here as the maximum altitude minus the minimum altitude of the basin). The graben shoulders as well as the adjacent cratonic platform reach comparably low elevations between 1500 and 2500 m a.s.l., and the flat graben floor is situated at altitudes between 600 to 1400 m a.s.l. (see Figure 1).

[6] The tectonic stress regime of the study area is extensional, but with local slight strike-slip components occurring. Strain is concentrated along narrow rift zones with relative motion of ~2 mm/yr to the East for the Victoria plate, i.e., the micro-plate between the eastern and western rift branches [*Calais et al.*, 2006; *Stamps et al.*, 2008]. Apart from minor volcanic activity, recent tectonic activity is witnessed by a large number of seismic events recorded during the last 5 years by a seismic monitoring network positioned around the Rwenzori block [*Lindenfeld et al.*, 2010]. Up to 800 events per month of magnitudes 1 to 4 occur at depths up to 25 km, mainly in intraplate positions on the eastern rift shoulder, but also scattered in the vicinity of the normal fault planes bounding the Rwenzori fault block and rift shoulder [*Lindenfeld et al.*, 2010; *Maasha*, 1975]. However, there are only a small number of earthquake foci beneath the Rwenzori fault block itself, except for a narrow E-W-oriented zone of earthquake foci located between the northern range and the southern block [*Lindenfeld et al.*, 2010].

[7] A flexural uplift pulse of the rift shoulder around 14–12 kyr before present (BP) [*Ring*, 2008; *Pickford et al.*, 1993] probably led to a fluvial network re-organization of the platform region. This tectonic pulse had a large-scale impact on the hydrological system by locally modifying base level and transport energy [*Pickford et al.*, 1993]; in detail, the northeastern basins draining the platform were probably affected by a non-quantifiable admixing of material from alluvial channels that were drained prior to channel network re-organization.

2.2. Lithology and Rock Properties

[8] Bedrock lithologies of the Rwenzori block and the rift shoulder consist of mainly Precambrian metamorphic rocks, such as gneisses, intercalated schists, and amphibolites (for the extent of amphibolite see Figure 1; geologic map in Figure 3), belonging to the Proterozoic Toro-belt and to the Archean basement of the Congo and Tanzania cratons [*Bauer et al.*, 2010]. Apart from the amphibolite (SiO_2 38–52 weight %), bedrock lithologies all contain quartz (SiO_2 is in a range between 57 and 83 weight % (B. Nagudi, unpublished data, 2010). In the northern range and on the rift shoulder, undifferentiated gneisses dominate, and in the southern part, gneisses with intercalated schists crop out (Figure 3).

[9] In the Albert Rift area, deep weathering of the pre-weathered basement surface has progressed since the Middle Miocene [*Bishop and Trendall*, 1966]. A mid-Cretaceous to early Miocene uplift period lead to stripping of parts of the weathered surfaces but mostly did not reach down to bedrock level [*Ollier*, 1959; *Taylor and Howard*, 1998]. The low-topography, slightly southward sloping platform between Lake Victoria and the Albert Rift valley today is characterized by thick lateritic, highly weathered saprolites and soils

[*Bishop and Trendall*, 1966; *Taylor and Howard*, 1998] and the occurrence of swamps.

[10] Mountain-scale bedrock strength may influence erosion [*Kühni and Pfiffner*, 2001]. Quantitative rock strength data for Albert rift lithologies are not available; instead, we give a qualitative characterization of the Precambrian rocks based on standard erodibility values of *Kühni and Pfiffner* [2001] and consider the rock mass strength (RMS) values published by *Korup and Schlunegger* [2009]. Generally, the basement rocks can be roughly classified assuming medium erodibility for the different schist units, low erodibility for the gneisses and very low erodibility for the amphibolites. Furthermore, compared with the above mentioned standard values, high-grade gneisses (as present in the Rwenzoris) possess high tensile strengths and therefore generally have high erodibility coefficients [e.g., *Johnson*, 1972]. However, besides lithology, the in situ rock stress regime in a rock mass, i.e., the mountain scale rock strength, can contribute significantly to the actual rock properties, as tectonically stressed and deformed rocks can have considerably reduced RMS values [*Augustinus*, 1995; *Montgomery*, 2001].

2.3. Glacial History of the Rwenzoris

[11] The recent topography of the Rwenzori block (Figures 2 and 3) has been shaped by several glaciations, which can be correlated to equivalent stages on Mt. Elgon and Mt. Kilimandjaro. The last three maxima date back to ~300 kyr, ~100 kyr, and 22 to 15 kyr (LGM), and one retreat stadium is reported at 11.6 kyr BP, corresponding to the so-called Katabarua, Ruimi Basin, Mahoma Lake, and Omirubaho stages, respectively [*Osmaston*, 1989; *Osmaston and Kaser*, 2001; *Hastenrath*, 2009]. Three southeastern mountainous basins (Table 2: 373, 388, and 491) were directly affected by glaciations (i.e., during the cosmogenic apparent age) and covered by ice to up to 40% during the Mahoma Lake (LGM) stage. Ice cover during the Omirubaho stage (11.6 kyr ago) amounted to 1.1%, 9.9%, and 13.3%, respectively. The recent Lac Gris stage (300 yrs BP to today) [*Osmaston*, 1989] has a comparably small extent: in 1995, its extent amounted to 1.5 km^2 [*Osmaston and Harrison*, 2005]. Until 2003, glacial recession continuously reduced this area to 0.96 km^2 [*Taylor et al.*, 2006]. Today's glaciers are even smaller and affect only the highest parts of basin 373 with an areal extent of <0.5% of the basin. Today, steep glacier tongues reach down to ~4600 m a.s.l., but are producing minor amounts of eroded material when compared with moraine remnant material of the earlier glaciation stages [*Young and Hastenrath*, 1987; *Osmaston*, 1989; *Osmaston and Harrison*, 2005; *Hastenrath*, 2009]. The glacial melt-water contribution to Mubuku River (basin 373) amounts to <2% of the total rivers' discharge [*Taylor et al.*, 2009].

[12] Due to repeated erosive ice cover (e.g., 260 km^2 during the Last Glacial Maximum, LGM [*Taylor et al.*, 2009]), characteristic U-shaped valleys with oversteepened walls and locally overdeepened basins occur down to altitudes of 2900 m a.s.l. (Figure 2). Based on geomorphological analyses of the landscape, several authors have suggested that the rugged topography of the eastward-tilted Rwenzori horst does not seem to have existed prior to the oldest Katabarua glaciation stage [e.g., *Taylor and Howard*, 1998; *Kaser and Osmaston*, 2002; *Ring*, 2008].
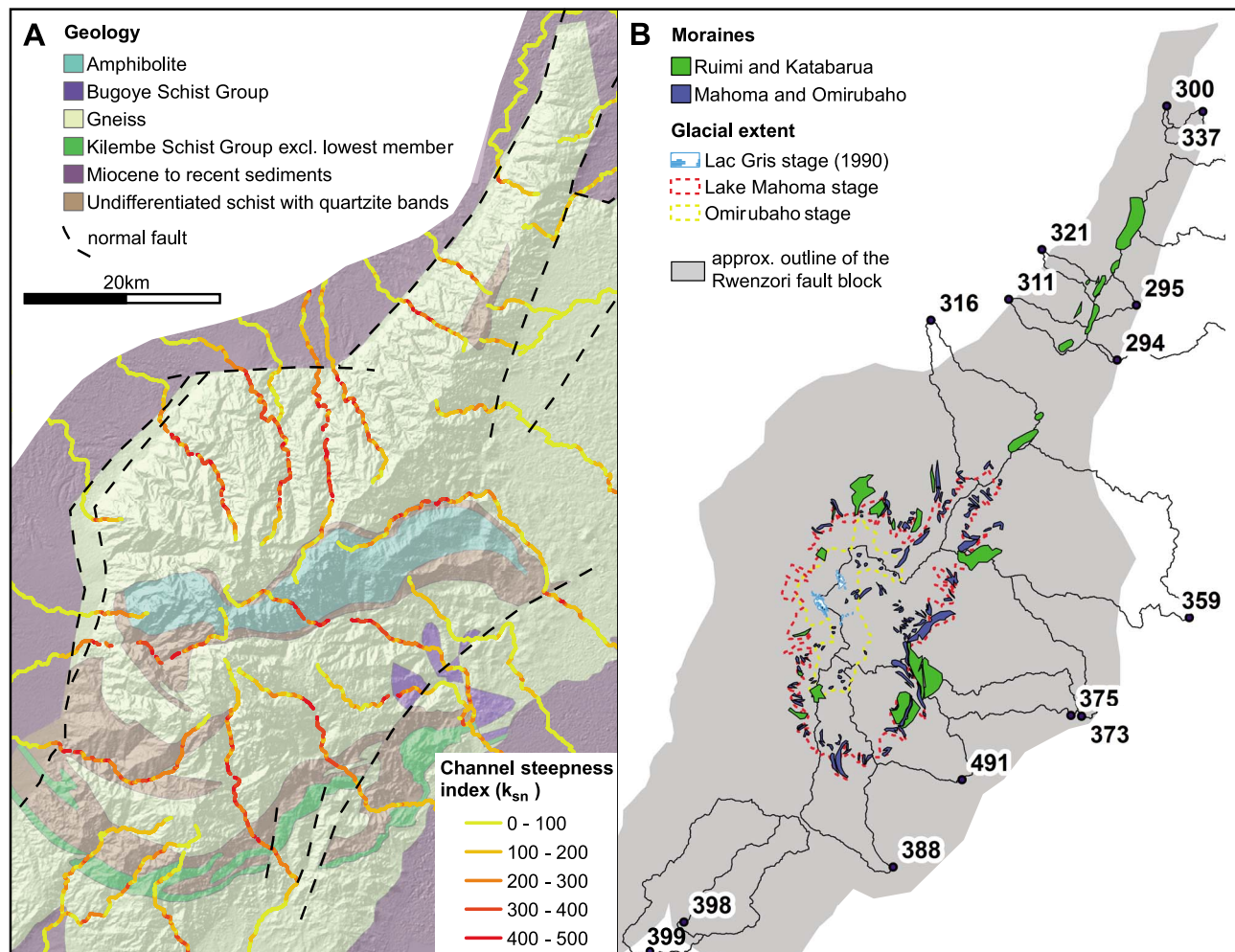
Figure 3. (a) DEM of the Rwenzori Mountains (including the Congo side) with continuous channel steepness (k_{sn} calculated using a reference concavity index $\theta_{ref} = 0.45$) along the main rivers and geological map showing main lithologies and major normal faults (after *Bauer et al.* [2010] and *Koehn et al.* [2007]). (b) Simplified overview map of the Rwenzori block and investigated catchments with todays' relicts of moraine material (Ruimi plus Katabarua stages and Mahoma Lake plus Omirubaho stages) and outlines of recent Lac Gris, and former LGM (Mahoma Lake) and Omirubaho (11.6 kyr) ice extents based on *Kaser and Osmaston* [2002].

[13] Large amounts of material from superimposed moraine generations related to the three older glaciation stages are still stored along the valleys above 2070 m a.s.l. [*Kaser and Osmaston*, 2002; *Osmaston and Harrison*, 2005]. This storage is attributed to the lack of pronounced melting seasons, which, in non-tropical glaciated areas, would ensure intermittently higher transport energy [*Kaser and Osmaston*, 2002]. Most catchments except a few basins with low maximum altitude and the platform and rift shoulder basins are affected by storage of moraine material, but very limited fluvial re-working of this old glacial material is indicated.

2.4. Climate and Vegetation

[14] Modern climatic conditions are humid to wet, with a locally varying mean annual rainfall between 800 and 1500 mm/yr on the rift shoulder and in the lowlands, which occurs during two rainy seasons [*Osmaston*, 1989; *Pickford et al.*, 1993; *Taylor et al.*, 2009]. However, these fluctuations between the seasons are far less pronounced in the mountains than in the lowlands [*Young and Hastenrath*, 1987; *Osmaston*, 1989; *Taylor et al.*, 2007]. Due to the high altitude and prominent position of the Rwenzori Mountains, the lower atmosphere's circulation is disturbed and rain-clouds are retained. The resulting constant orographic cloud cover produces all-year-round daily precipitation on the eastern flank of the Rwenzori Mountains, causing minor annual bimodal fluctuations and typical "montane cloud forest" conditions [*Foster*, 2001; *Hamilton*, 1995; *Kappelle*, 2004].

[15] On the eastern flank of the Rwenzori Mountains, precipitation and temperature follow a gradient with altitude: at the base of the mountains at 1250 m a.s.l., precipitation amounts to 1150 mm/yr and the mean annual temperature is ~24°C. At 3300 m a.s.l. values of 2600 mm/yr and 10–15°C are reached, and above that altitude, precipitation decreases again to 2000 mm/yr at 4000 m a.s.l. and temperature drops

Table 2. Sample Specific and Basin Characteristics

| River	Sample	UTM-Latitude (°N)	UTM-Longitude (°E)	Basin Area (km²)	Min. Elevation (m a.s.l.)	Mean Elevation (m a.s.l.)	Max. Elevation (m a.s.l.)	Basin Average Relief[a] (m)	Mean Hillslope Gradient[b] (°)	Channel Steepness Index[c] k_{sn}	Concavity Index[d] (θ)	Glacier Ice Cover — Mahoma Lake Stage 22–15 kyr (%)	Glacier Ice Cover — Omirubaho Stage ~11 kyr (%)	Moraine Cover — Moraine >100 kyr (%)	Moraine Cover — Moraine <22 kyr (%)	Vegetation Cover of Basins — Forest, Shrubs (%)	Vegetation Cover of Basins — Grassland, Agriculture, Swamp (%)	Vegetation Cover of Basins — Bare Rock (%)
Northern Mountainous Catchments																		
Mahoma	294	0.5909	30.1455	1	1786	2121	2604	335	21.7	-[e]	-[e]	0	0	0	0	34.5	65.1	0
Dunga	295–1 and 295–2	0.6556	30.1658	11.50	1699	2206	2854	507	22.9	149	0.5100	0	0	4.5	0	66.3	33.6	0
Sempaya	300	0.8071	30.2334	1	1030	1537	1662	507	13.8	-	-	0	0	0	0	53.1	16.7	0
Rugo	311a and 311b	0.6610	30.0479	18.7	970	2242	3069	1272	23.7	201	-0.0028	0	0	7.2	0	95.7	3.8	0.5
Rutoba	316	0.6411	29.9765	89.9	891	2408	3802	1517	22.2	212	0.2500	0	1.9	3.0	0.5	88.2	11.1	0.7
Humiya	321	0.7119	30.0799	9.5	947	1767	2637	820	19.5	149	0.0500	0	0	9.1	0	62.5	28.6	0.1
Itojo	337	0.8358	30.2265	7.5	991	1326	1736	335	18.8	64	0.5800	0	0	0	0	27.6	19.8	0
Southern Mountainous Catchments																		
Ruimi	359	0.3650	30.2150	265.6	1017	2045	3984	1028	16.4	183	0.2900	0	6.4	0.9	1.5	51.4	48.0	0.2
Mubuku	373–1 and 373–2	0.2604	30.1209	255.1	1121	2855	5015	1734	21.6	237	0.3600	43.1	13.3	2.5	3.9	72.6	17.4	9.9
Isebo	375	0.2667	30.1095	50.5	1122	2072	3580	950	17.7	163	0.1100	0	0	8.2	0	56.9	42.7	0.2
Nyamagasani	388a and 388b	0.1231	29.9498	95.2	1343	3036	4575	1693	23.9	229	0.0730	41.7	9.9	4.8	0.8	82.5	6.6	10.9
upper Lubilia	398	0.0808	29.7487	60.2	1034	2075	3321	804	17.5	168	0.3000	0	0	0	0	-	-	-
Lubilia	399	0.0405	29.7200	160.9	1033	1839	3321	806	16.9	128	0.5000	0	0	0	0	56.2	43.8	0.0
Nyamwamba	491	0.2134	30.0054	96	1384	2947	4398	1563	23.9	239	0.0600	44.4	1.1	7.3	4.2	83.9	9.4	6.5
Platform Catchments																		
northern Mpanga	9	0.6431	30.3931	296.2	1355	1617	2959	262	8.6	80	0.6000	0	0	0.4	0	-[e]	-	-
southern Mpanga	28	0.1008	30.4615	124.8	1234	1417	1598	220	8.6	17	0.0910	0	0	0	0	36.9	62.1	0.3
Dura	24	0.9014	30.3393	5202.9	1136	1356	3003	183	6.1	-	-	0	0	0	0	-	-	-
Rift Shoulder Catchment																		
Wasa	538	0.4588	30.3798	320	562	1211	2450	649	11.3	107	0.6600	0	0	1.8	0	23.6	75.7	0.1

[a] Basin average relief = mean elevation − minimum elevation.
[b] Hillslope gradient is the mean ±1σ of all slope values within the entire catchment.
[c] Stream channel gradient normalized to drainage area (following *Wobus et al.* [2006]) and description in section 3.2.
[d] Mean of undisturbed river segment.
[e] No values calculated for this basin.
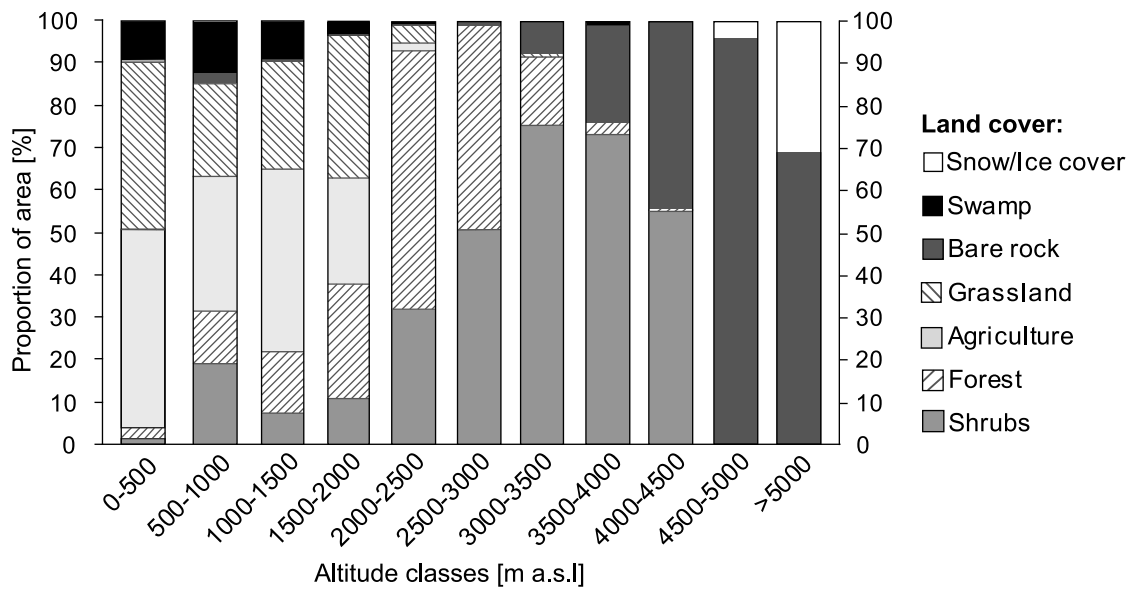
Figure 4. Proportions of land cover types for each 500 m-spaced altitude class integrating over the area covered by the map of Figure 1. The land cover type "shrubs" contains both savannah-type and bushy vegetation of the lowlands and lower mountainous regions (<3000 m a.s.l.) and represents typical afroalpine belt-type evergreen vegetation in the high-altitude regions (>3000 m a.s.l.).

to 4–10°C. Above 4300 m a.s.l., precipitation is mainly received as snow, average temperatures are below 4°C and reach 0°C at 4600 m a.s.l. [*Osmaston*, 1989].

[16] The long-term climatic record for the study area (based on pollen records) suggests warm tropical climate similar to today prior to 42 kyr BP, a change to cooler and drier conditions until 30 kyr BP, followed by a period of cool and moist climate during the LGM period [*Coetzee and van Zinderen Bakker*, 1989; *Johnson et al.*, 1996]. The minimum age of deglaciation dates back to 16 kyr BP [*Livingstone*, 1967] and the post-LGM climate was warm and humid from ~12.5 to ~4 kyr [*Taylor and Howard*, 1998] becoming increasingly dry from ~4 kyr BP onwards [*Marchant and Hooghiemstra*, 2004; *Kiage and Liu*, 2006; I. Ssemmanda, personal communication, 2009], with a grassland expansion around Lakes Albert and Victoria, indicating aridification at around 4.2 kyr BP [*Marchant and Hooghiemstra*, 2004].

[17] Extensive vegetation cover and montane forest succession commenced in post-LGM times [*Livingstone*, 1967]. Present-day vegetation has been established since the retreat of the Omirubaho glaciation stage [*Livingstone*, 1967]. The vegetation pattern observed in lowland areas is a mixture of agricultural land use, forests, swamps, savannah (classified as shrubs in land cover analysis, Figure 4), and grasslands (see Table 2). In the Rwenzori Mountains, vegetation is a mixture of agricultural land, forests, swamps, and savannah. Here, the vegetation pattern is characterized by altitudinal zonation, resulting from the combination of vertical (rain) and horizontal (cloud-filtered) precipitation [*Stadtmüller*, 1987; *Foster*, 2001] that ensures optimum conditions for growth of vegetation under mountain cloud forest conditions. The United Nation's Food and Agriculture Organization (FAO) characterized the woody biomass of the Rwenzori Mountains with a value of 2–3 t/km^2, which is a value comparable to e.g., the densely vegetated Congo Basin lowlands,

where average values of 2–4 t/km^2 prevail [*Food and Agriculture Organization of the United Nations*, 2000].

[18] Generally, an absence of bare rock zones is rarely encountered in glaciated settings and contrasts to e.g., Mount Kilimanjaro and Mount Kenya [*Young and Hastenrath*, 1987]. In the Rwenzoris, bare rock exposures are almost exclusively limited to slopes in regions above 4000 m a.s.l. (Figure 2), because remnant glacial and fresh rockfall material on valley floors is quickly covered by vegetation in the time span of a few years (own observation, *Temple* [1968], and *Bauer et al.* [2010]) and even the steep flanks of huge valley moraine bodies of the former glaciations are covered by dense vegetation (Figure 2c).

[19] From field observations, we estimate soil thickness to be ~300 cm in areas up to 3000 m a.s.l. and 20 to 100 cm up to an altitude of 4200 m a.s.l.. The notably convex shaped soil-mantled hillslopes feature both a large hydrological storage capacity in the thick regolith cover, and a low landslide density, respectively [e.g., *Allison*, 1994] – two facts consistent with our own field observations (e.g., Figures 2a and 2c). In the platform areas, deep in situ weathering produced regolith thicknesses of 5–15 m, even up to 30 m in some areas [*Bishop and Trendall*, 1966; *Taylor and Howard*, 1999].

3. Methods

3.1. Sample Preparation and AMS Measurements

[20] We sampled 13 perennial rivers for cosmogenic [10]Be analysis on the Ugandan part of the Rwenzori Mountains, one on the adjacent rift shoulder and three on the platform from active channel bars (Figure 1 and Table 1). Quartz was extracted using HF leaching methods and magnetic separation. [10]Be was extracted using standard methods [*von Blanckenburg et al.*, 1996; *Wittmann et al.*, 2007], and about 200 μg of [9]Be carrier derived from a Phenakite mineral were added to each sample. [10]Be/[9]Be ratios were

measured in BeO targets with accelerator mass spectrometry at SUERC in East Kilbride and corrected as described by *Maden et al.* [2007]. The ^{9}Be Phenakite-carrier was determined to contain a ^{10}Be/^{9}Be ratio of $4.5 \pm 1.6 \times 10^{-15}$ at SUERC AMS laboratory. Samples 295–2 and 373–2 were measured at ETH Zurich and corrected according to *Kubik and Christl* [2010]. Results from both AMS laboratories are directly comparable; SUERC reports absolute ^{10}Be/^{9}Be ratios derived from using a nominal ratio of 3.06×10^{-11} for their NIST reference material (National Institute of Standard and Technology Standard SRM4325 as reported in *Xu et al.* [2010]), a value that has also been measured for this material at ETH. We decided to reduce all measured ^{10}Be/^{9}Be ratios (also blank ratios, accordingly) by a factor of 1.096 as suggested by *Kubik and Christl* [2010] to allow for direct comparison with data obtained relative to the standards produced by *Nishiizumi et al.* [2007]. These standards are often used as reference standards in the Cronus online calculator and are compatible with the newly determined ^{10}Be half-life ($1.387 \pm 0.012 \times 10^{6}$ yr) [*Chmeleff et al.*, 2010; *Korschinek et al.*, 2010]. Analytical as well as blank error corrections are described in Table 1.

[21] In order to check the comparability between the samples and also between SUERC and ETH AMS, duplicates of the 0.5–1.0 mm size fraction of samples 295 and 373 were measured at both AMS laboratories. Within 1σ uncertainty (see Table 1), ^{10}Be concentration results agree for 373–1 and –2, and an overlap within both uncertainties is given for 295–1 and –2. Consistency for grain sizes was explored by measuring both the 0.5–1.0 mm and the 1.0–1.25 mm size fractions of samples 311 and 388. For two catchments and their sub-basins (24- Mpanga S and 9-Mpanga N, and 399-Lubilia with 398-upper Lubilia) (see Table 1), we tested catchment-wide consistency of the results with regard to drainage area changes.

3.2. Production Rate Corrections

[22] Calculations of production rates (using pixel-based altitudes derived from 30 m resolution DEM from the Advanced Spaceborne Thermal Emission and Reflection Radiometer ("ASTER") satellite data) and absorption laws for ^{10}Be including muons were done following *Schaller et al.* [2002] and ^{10}Be sea level high latitude (SLHL) production rates of 4.5 ± 0.5 for high-energy neutrons, 0.097 ± 0.007 for negative muons, and 0.085 ± 0.012 for fast muons were used. The ^{10}Be SLHL production rate for high-energy neutrons was recalculated from *Balco et al.*'s [2008] ^{10}Be calibration-site data set, using the time-independent altitude-latitude scaling scheme of *Dunai* [2000] and a ^{10}Be half-life of 1.387 Myr [*Chmeleff et al.*, 2010; *Korschinek et al.*, 2010]. The ^{10}Be SLHL production rates for muons were taken from *Kubik et al.* [2009].

[23] Production rates were corrected for topographic shielding following *Norton and Vanacker* [2009]. The topographic shielding factors were calculated from DEM-derived basin-specific elevation variances and the calculated theoretical maximum shielding factor [*Norton and Vanacker*, 2009]. Corrections of the production rate due to snow- and ice- related shielding were carried out following *Wittmann et al.* [2007], by setting the nucleogenic component of the production rate to zero for pixels covered by ice due to recent

glaciation. The extent of recent glaciation was digitized from the 'Map of the Rwenzori Mountain National Park' [*Kaser and Osmaston*, 2002]. We calculated the respective glaciated areas during Mahoma and Omirubaho stages for affected basins (see Table 2), based on known equilibrium line altitudes (ELA) and on the location of terminal moraines (shown in Figure 3b) [*Osmaston and Harrison*, 2005]. For pixels covered by snow, a correction factor was calculated based on *Wittmann et al.* [2007, equation 5], using a snow density of 0.3 g/cm^3 for old, compacted snow [*Roebber et al.*, 2003]. We did not specifically correct for varying quartz contents within the different basins, except in cases of basins 359 and 373, where the total production rate was set to zero for pixels covered by large outcrops of amphibolite with negligible quartz contents (see Figure 1). Production rate correction factors (for topographic shielding, snow and ice shielding, and different quartz contents) vary between 0.87 and 0.99 for the sampled basins (see Table 1). The above-described corrections were carried out in accordance with our understanding of current treatment of cosmogenic nuclide data. However, given that production rate calibration sites at low latitudes are poorly represented in most scaling models, muonic production and their depth-scaling is still not well understood, and snow and ice cover may have fluctuated significantly in the past, we adopt an overall production rate uncertainty of 10% and deliberately neglect a correction for changes in the production rate over time due to changes in Earth's magnetic field.

3.3. Numerical Modeling of the Approach of Cosmogenic Nuclides to Steady State After Surface Zeroing by Glaciations

[24] We explore the effects of former glaciation on TCN-derived denudation rates by using a modeling approach, similar to the approach used by *Wittmann et al.* [2007] that is based on the numerical model by *von Blanckenburg* [2005]. ^{10}Be production is thereby simulated by integrating over the attenuation path length during small time steps, while the surface is lowered by denudation. We used the muonic and nucleogenic production and adsorption terms from *Schaller et al.* [2002] for calculation, and our revised total SLHL production rate. Starting at 100 kyr BP, we simulated the response of denudation to three de-glaciation events by assuming a prescribed ("input") denudation rate of 300 mm/kyr following the Ruimi Basin stage glaciation (see Figure 5), and a rate of 200 mm/kyr for both the Mahoma Lake and the Omirubaho stages beginning at 22 kyr and 11.6 kyr BP, respectively. We chose a higher input denudation rate for Ruimi Basin stage, as this glaciation presumably lasted longest, thus removing most surface material. In between glaciations, input denudation rates approach ~50 mm/kyr, an average value that has been measured in northern basins of the Rwenzoris that were never affected by the two youngest glaciations stages (case 1, lower gray bar). The modeled or "real" denudation rate that approaches steady state after the glacial perturbations, but never quite reaches it (case 2), is denoted by the black stippled line in Figure 5.

3.4. Geomorphologic Analysis

[25] For topographic analysis, an ASTER-DEM with a resolution of 30 m was used. To create a hydrologically
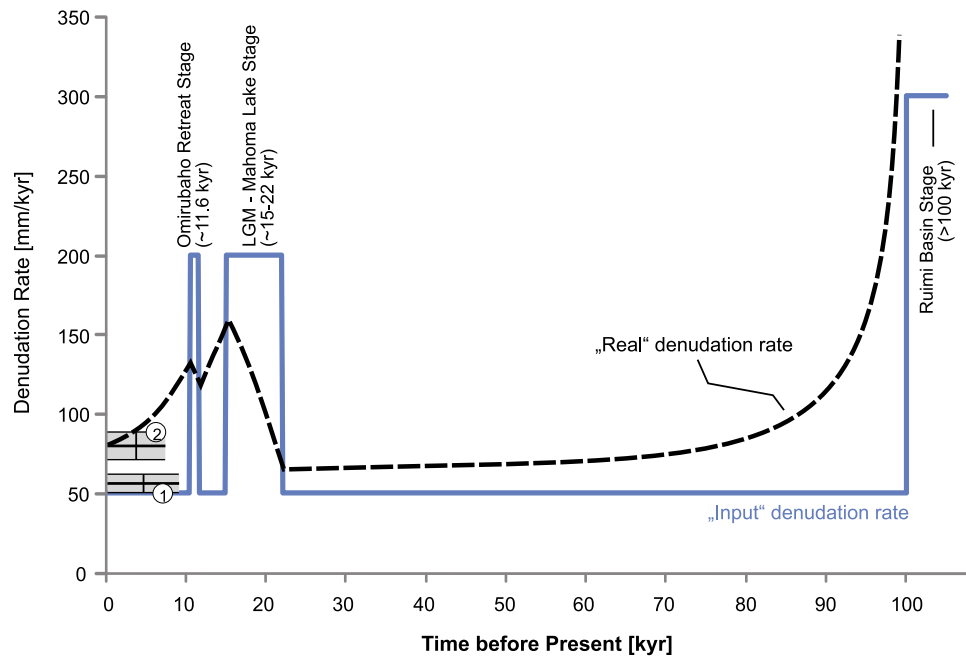
Figure 5. Numerical modeling of the approach of cosmogenic nuclides to steady state after zeroing by glaciations (similar to the approach used by *Wittmann et al.* [2007]) for the last 100 kyr before present (BP). Starting at 100 kyr BP, an input denudation rate (see blue curve) of 300 mm/kyr during the Ruimi Basin glaciation was assumed. In between glaciations, denudation rates approach an input, or steady state denudation rate of ~50 mm/kyr, an average value that has been measured in northern basins of the Rwenzoris that were never affected by the two youngest glaciations stages (case 1, lower gray bar). During the LGM stage (~15–22 kyr BP) and the last glacial retreat stage (Omirubaho, at ~11.6 kyr BP, assumed here to have lasted 1 kyr) an input denudation rate of ~200 mm/kyr was assumed. The black stippled curve gives the "real" (or modeled) denudation rate that approaches steady state denudation after the glacial perturbations. The analysis shows that cosmogenic steady state erosion is not achieved in this scenario; i.e., real denudation after the last perturbation amounts to ~80 mm/yr. Case 2 (upper gray bar) denotes the average measured denudation rate in formerly glaciated Rwenzori mountainous basins (~80 mm/kyr) that falls between the blue and the stippled curve, indicating that measured denudation rates are close to steady state, but do not quite approach it. In case of this scenario, where complete zeroing of surface concentrations within an entire basin is simulated, TCN-derived denudation rates overestimate real rates by ~50%.

correct DEM, the ArcGIS pit-filling routine was used. We calculated the stream network and catchment areas via an eight direction flow model from the DEM. We extracted morphological parameters (Table 2) from the DEM via standard ArcGIS routines. Hillslope gradient is the maximum rate of change between each cell and its neighbors averaged over the whole basin. We also calculated mean hillslope gradients for areas of similar basement lithology across the mountainous basins using the geological map in Figure 3. As we used a DEM with 30 m resolution, a difference of few degrees compared with other studies where 10 m resolution DEM data was used can be assumed. The hillslope histograms (Figure 6) were calculated by ArcGIS for the catchment areas as outlined in Figure 1.

[26] River profiles were derived from the DEM using a 250 m smoothing window and a 15 m contour interval (Figure 7). The geomorphologic analysis of river channels was done following the method described by *Wobus et al.* [2006], using freely available Matlab and ArcGIS scripts (www.geomorphtools.org). To smooth the river profiles and minimize data noise while keeping the form of the profile, a moving window of 250 m edge length and 15 m contour

steps were chosen. Channel steepness (k_s) and concavity (θ) were calculated by linear regression within log-log slope-area plots of the river profiles. Because of the self-correlation of k_s and θ, a direct comparison of channel steepness among basins with different concavity index is problematic [*Wobus et al.*, 2006]. For adequate comparison we calculated a normalized channel steepness indices (k_{sn}) from the θ-values of the undisturbed river segments (see Table 2), using a reference concavity θ_{ref}. θ_{ref} can be computed using the mean θ of all undisturbed river segments within a region but can also be freely chosen without altering the relative differences in k_{sn} [*Wobus et al.*, 2006]. To allow comparison with other studies [e.g., *Wobus et al.*, 2006; *Ouimet et al.*, 2009; *Cyr et al.*, 2010; *Schildgen et al.*, 2012], θ_{ref} was defined as 0.45. The continuous k_{sn} values were then combined with lithological maps and compared to glacial ELA as well as the maximum extents of glacial ice-coverage (Figure 3).

3.5. Glacial and Landcover Analysis

[27] Based on the map from *Kaser and Osmaston* [2002], we quantified the areal cover of remnant moraine material for the two combined oldest and youngest glaciation stages
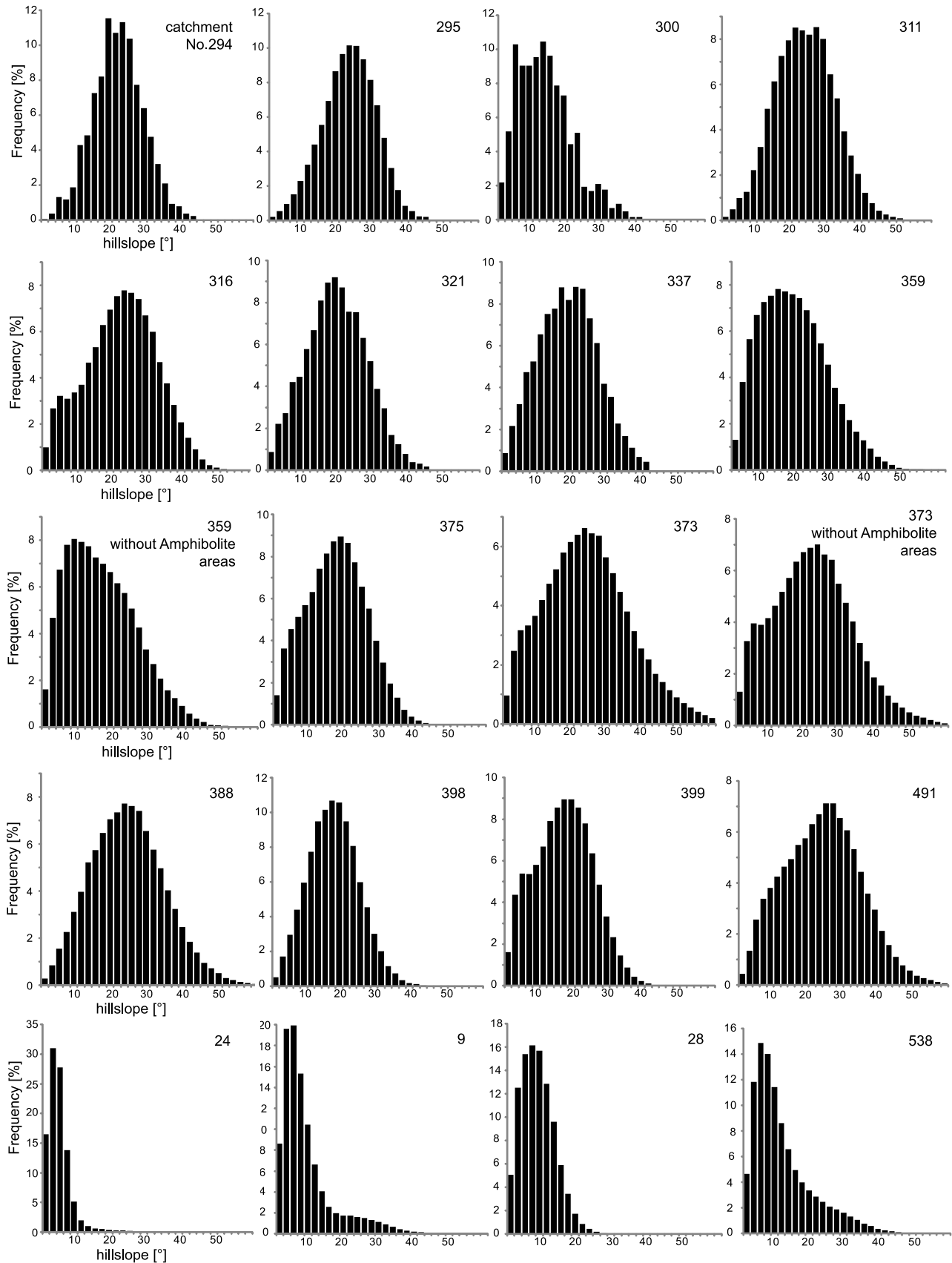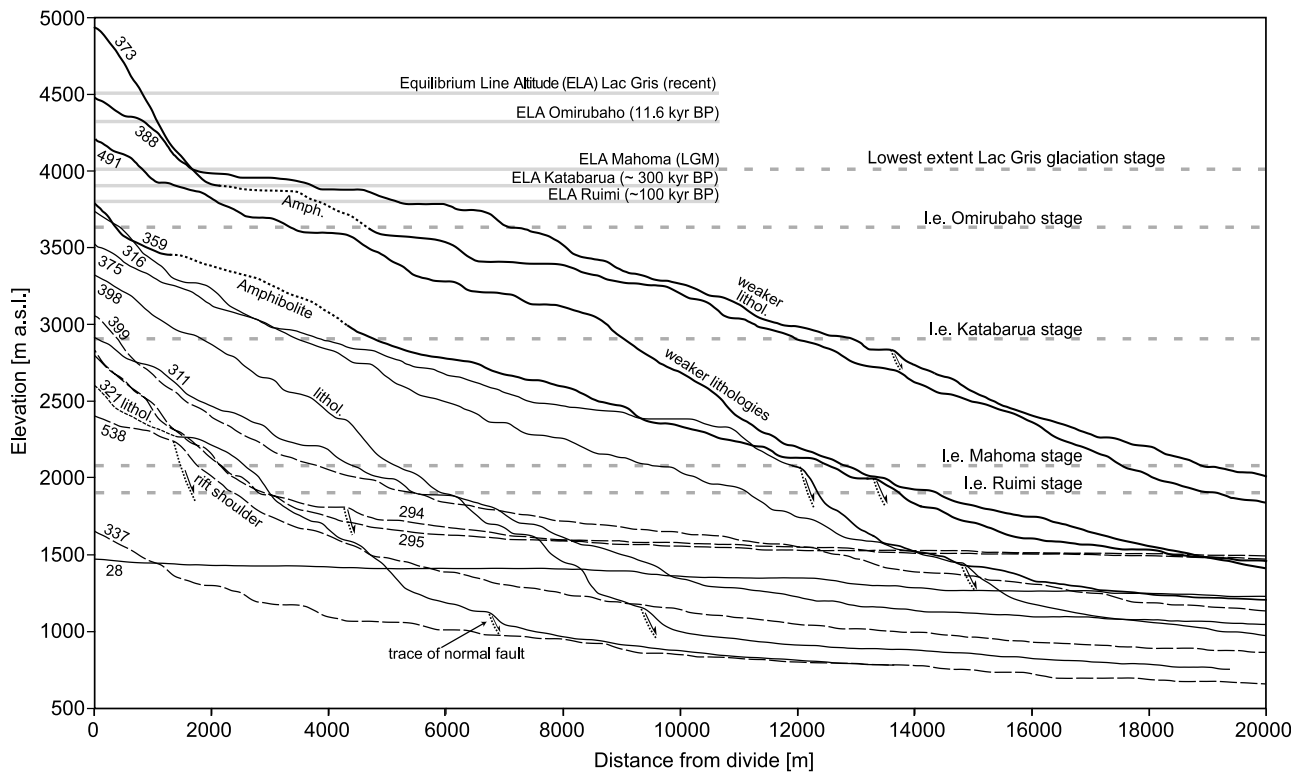
Figure 6. Hillslope distribution histograms calculated for the investigated basins calculated from 30 m DEM. For catchments 373 and 359 we also calculated hillslopes for basin area excluding the amphibolite.

Figure 7. River long profiles of sampled rivers (catchment numbers given) draining the Rwenzori Mountains that were also analyzed for cosmogenic nuclides, calculated from a 30 m resolution DEM using a 250 m smoothing window and a 15 m contour interval. Solid lines: mainly concave shaped river profiles, stippled lines: mainly convex shaped river profiles. Equilibrium line altitudes (ELA) and maximum ice extents are indicated for all 5 glaciation stages (following *Kaser and Osmaston* [2002]). Where knickpoints can be assigned to major faults (NF = normal fault) or lithological changes, this is indicated. Extents of erosion-resistant Amphibolite are indicated with dotted lines (basins 359 and 388).

(for Ruimi plus Katabarua and for Mahoma plus Omirubaho; see Figure 3b and Table 2).

[28] In order to classify the recent landcover of the study area (Figure 4), we used the three bands in the visible and near infrared (VNIR) from ASTER satellite data with a resolution of 15 m. The three individual bands were stacked using the model maker tool in ERDAS IMAGINE 9.1 in order to create a multiband image. To enhance the visual interpretability, we utilized the histogram equalizer and tasseled cap transformation (spectral enhancement). Eight different output classes were analyzed from the image by the 'supervised classification' tool of the ERDAS IMAGINE 9.1 classifier. Correction for the landcover was done by referring to field observations and Google Earth images. According to the climatic conditions of the region, agricultural areas above 2500 m a.s.l. were corrected to be shrubs. Areas classified as swamps at an altitude above 4200 m a.s.l. were corrected to be bare rock areas.

4. Results

[29] Measured denudation rates range from 7.8 to 131 mm/kyr (Tables 1 and 2 and Figure 1). According to topographic, morphological, and structural aspects, our data set can be subdivided into three groups:

[30] **Group 1.** The northern mountainous catchments (see Tables 1 and 2) drain the flanks of the simple horst-structure of the narrow northern range of the Rwenzori block. Also included in this group is basin 538 (rift-shoulder catchment in Tables 1 and 2) that partly drains the Rwenzori block, but most of the catchment area is located on the rift shoulder. Group 1 basins erode at rates between 28.2 ± 3.3 and 70.0 ± 8.6 mm/kyr (n = 10 measurements, mean 51.6 ± 1.8 mm/kyr, standard deviation SD = 12.4 mm/kyr) and have a mean relief of ~750 m.

[31] **Group 2.** The southern mountainous catchments (see Tables 1 and 2) drain the high relief central part of the Rwenzoris with denudation rates ranging between 32.3 ± 4.0 and 131 ± 21.2 mm/kyr (n = 9, mean 71.8 ± 3.5 mm/kyr, SD = 36.8 mm/kyr). Two basins erode at higher rates of >100 mm/kyr (basins 388 and 491). For all catchments draining the Rwenzori block (group 1 and 2), denudation rates range between 28.2 ± 3.3 and 131 ± 21.2 mm/kyr, at an average relief of ~1200 m (Table 2).

[32] **Group 3.** The low-topography platform catchments drain the eastern rift shoulder, which have a mean relief of ~200 m. Here, denudation rates lie between 7.8 ± 0.9 and 17.7 ± 2.1 mm/kyr (n = 3, mean 11.6 ± 0.1 mm/kyr, SD = 5.4 mm/kyr). This group includes basin 9 that has some westerly tributaries reaching up to the northeastern
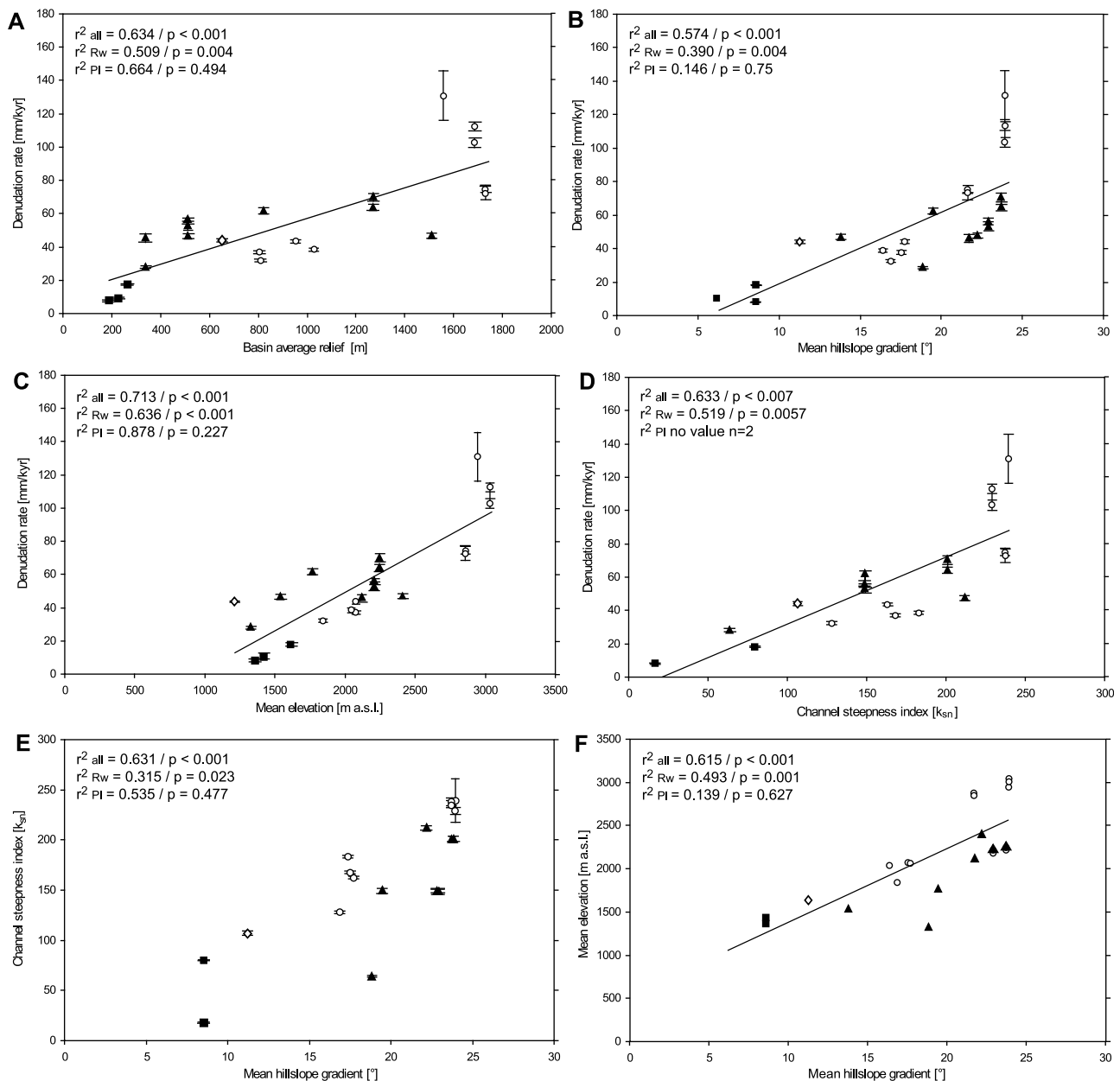
Figure 8. Cosmogenic nuclide-derived denudation rates (mm/kyr) versus (a) basin average relief in m a.s.l., (b) mean hillslope gradient of basins in degrees, (c) mean elevation (m a.s.l.) and (d) channel steepness index. Also plotted are (e) channel steepness index versus mean hillslope gradient and (f) mean hillslope gradient versus mean elevation. The r^2_{all} values give correlation coefficients for all catchments, r^2_{Rw} for mountainous catchments and r^2_{Pl} for all platform catchments, regressions refer to all data points. The sampled basins are divided into 4 groups: squares = rift shoulder platform, triangles = northern Rwenzori block, circles = southern Rwenzori block, rhombohedra = rift shoulder. Denudation rates of basins 373, 388, and 491 may be overestimates due to glaciation effects (see Section 5.2.1), and thus, Figure 8e might be reconciled toward a linear regression (statistics given for linear regression). The error bars correspond to the 'internal error' values given in Table 1.

Rwenzori flank, and has a slightly higher denudation rate of 17.7 ± 2.1 mm/kyr.

[33] Denudation rates measured in the Rwenzori Mountains and on the cratonic platform show positive linear correlations with basin average relief, mean hillslope gradient, mean elevation, and channel steepness index (Table 2 and Figure 8). Implications from the observed correlations will

be discussed in Section 5. Note that our denudation rates do not show any correlation with basin area, and that the following observed correlations between denudation and topographic parameters are not severely changed if the low-topography basins of the platform are excluded (see Figures 8a–8c).

4.1. Denudation Rates Versus Topographic Metrics

[34] Intrinsic in the positive correlation of denudation with topographic parameters is the correlation with mean annual temperature and precipitation. We observe highest denudation rates for the catchments with the highest maximum altitudes and mean elevations (basins 373, 388, 491). Generally, these basins show the highest values for all topographic parameters (see Figure 8). Basin hypsometries of these catchments yield 17%, 19%, and 23%, respectively, of the total drainage area present in the high altitude zone above 4000 m a.s.l. (compared to 4–0% for the other catchments). These basins erode at the highest observed rates of all mountainous catchments (mean rate of 107 mm/kyr, n = 5). Basin 373 has the highest maximum elevation (Table 2), but has a lower denudation rate and proportionally less area at high altitudes when compared with basins 388 and 491. However, the reasons for the high rates of the three above mentioned basins could be methodological, which will be discussed in a later section (Section 5.2).

4.2. Basin-Average Slope Gradients, Slope Histograms, and Lithology

[35] In many cases hillslope angles can be used as a proxy for the erodibility of the prevailing lithologies [*Hack et al.*, 2003]. However, for the Rwenzori Mountains, it has to be noted that the majority of slopes are soil-mantled and hence the hillslope gradient values are characteristic of a morphology resulting from a mixture of underlying bedrock and overlying regolith cover of variable thickness. Hence, the mean basinwide slope is a composite one that integrates over both soil-mantled, and, where present (e.g., basins 373, 388, 491), over bedrock-covered slopes. The skewness of hillslope distributions, which we present for our basins in Figure 6, can give an indication on the relative importance of erosional versus depositional processes and the occurrence of hillslope failures [*Wolinsky and Pratson*, 2005, section 5.5].

[36] In detail, calculated mean hillslope gradients for the different lithologies of the Rwenzori Mountains show that the gneissic areas exhibit steep slopes of 22.3°, and the intercalated undifferentiated schists with quartzite bands and the Kilembe Schist units feature lower average hillslope gradients of 20.9° and 18.7°, respectively. Only the amphibolite area (that we subtracted from further consideration for cosmogenic nuclide calculations) shows a higher average hillslope value of 26.3°. These minor differences in hillslope gradients correspond to the ranking of the lithologies according to general RMS values, where amphibolites are ranked as more resistant than gneiss, and schists yield the highest erodibilities.

[37] The overall linear correlation between slope and denudation (see Figure 8b) is only impaired by three outlying data points (basins 373, 388, 491). In these basins, we observe the largest proportions of steep slopes with values between 40° and 60°. These areas with very steep slopes cover 6 to 9% of the total basin areas of basins 373, 388, 491, respectively (see Figure 6). In basins draining the flat rift shoulder and/or graben areas (e.g., 9, 538), and in montane basins containing mountainous valleys that were filled during postglacial times to subhorizontal level by swamps (e.g., 359), we find positive skewness (Figure 6). In only few basins (e.g., 295), we observe negative skewness of hillslope distributions.

4.3. Channel Profiles and Steepness Indices

[38] As a potential indicator for tectonic activity driving river incision [*Safran et al.*, 2005; *Berlin and Anderson*, 2009], we extracted channel profiles (see Figure 7) and calculated continuous (Figure 3a) and basin-integrated channel steepness indices (k_{sn}) (Figure 8d). The latter parameter is a measure of stream-channel gradient normalized to drainage area [*Wobus et al.*, 2006] and therefore a proxy for river incision rate in glacially non-modified landscapes [*Cyr et al.*, 2010]. Apart from the linear correlation of k_{sn} with denudation rates (Figure 8d), channel steepness also correlates linearly with mean hillslope gradient (see Figure 8e).

[39] River profiles for most catchments (e.g., 311, 316, 373, 388, 491) are uneven to rough, showing the presence of a number of knickpoints. Potential causes for the existence of knickpoints in river profiles include litho-specific erodibility, tributary confluences, the structure and presence of active faults, base level changes, and overprinting by glacial erosion [*Whipple et al.*, 1999; *Brocklehurst and Whipple*, 2006; *Phillips and Lutz*, 2008]. In basins where lithology is partly uniform (e.g., 311, 316 with gneissic basement), these knickpoints are most likely related to tributaries (e.g., catchments 311) or are potentially caused by faulting and uplift. A clear relationship between a major fault and a strong knickpoint river morphology can be found in the lower part of river profile 375 (at *x* axis value 12,000 m). We will discuss these relations in more detail in Section 5.2.

4.4. Landcover Analysis

[40] From land cover analysis of the study area (Figure 4 and Table 1), it follows that >99% of the surface area below 3000 m a.s.l. is covered by a combination of grassland, agricultural land (up to 2500 m a.s.l.), forests, swamps, and shrubs. The 'shrubs' are represented by bushy savannah in the lowlands, and by typical afroalpine vegetation in the mountainous areas. The mountainous regions are mainly covered by montane forest and evergreen afroalpine vegetation. In altitude regions between 3000 and 4000 m a.s.l., bare rock area increases from 10 to 20% and reaches 50% between 4000 and 4500 m a.s.l. With respect to the individual catchments, the non-vegetated area is <1% for all catchments except 373, 388, and 491, for which bare rock areas account for 6 to 11% of the basin area (see Table 2).

5. Discussion

5.1. Relative Magnitude of Denudation in the Rwenzori Mountains

5.1.1. Mountainous Catchments Versus the Low-Relief Platform and Rift Shoulder

[41] The average denudation rate for low-relief basins exclusively draining the low-topography platform (i.e., basins 24 and 28) is 8.5 ± 1.0 mm/kyr. Comparing these low platform denudation rates with those of the high-relief basins (average 59.9 mm/kyr, group 1 and 2), the latter show 5- to sevenfold higher mean denudation rates. One explanation could be that the focus of uplift in the Rwenzori Mountains since Middle Miocene times (oldest syn-rift sediments in Rwenzori region [e.g., *Pickford et al.*, 1993]) that caused their orogenic evolution in the first place, is ongoing. Cosmogenic nuclides could thus well reflect ongoing differential

uplift and erosion in the mountains, and the near-absence of these processes in the lowlands. Beyond that, there is the higher potential for erosion in the mountainous basins, due to steeper slopes and large climatic gradients (including glaciation, frost shattering), when compared to the flat lowland areas.

5.1.2. Comparison With Other Settings

[42] In comparison with other tectonically active, high-relief settings of the world that have similar topography and comparable slopes, the mean denudation rate ($\sim$69 mm/kyr) of the measured mountainous Rwenzori basins is remarkably low. Qualitatively, other comparable, yet compressive settings erode at a rate that is on average $\sim$10 times faster: To name a few large-scale studies, medium-sized basins of the high Central Swiss Alps erode at rates of 500 to 1400 mm/kyr [*Wittmann et al.*, 2007; *Norton et al.*, 2010], the Central Andes erode at a mean rate of ca. 400 mm/kyr [*Safran et al.*, 2005; *Wittmann et al.*, 2009; *Insel et al.*, 2010], and the high Himalaya erodes at maximum rates of 3000 mm/kyr [*Vance et al.*, 2003; *Ouimet et al.*, 2009], with mean values, depending on lithology, topography, etc., between 230 to 360 mm/kyr [*Ouimet et al.*, 2009; *Palumbo et al.*, 2010]. In the mainly extensional setting of the Sierra Nevada, California, overall denudation rates, albeit constrained from very small basins (<1 km^2) with moderate relief, are much lower (20–30 mm/kyr). However, in the vicinity of active fault scarps and steep river canyons, erosion may peak at 250 mm/kyr in this setting [*Riebe et al.*, 2000]. In contrast, the mountainous Rwenzori basins erode at a rate that is similar to those derived from the retreating Sri Lankan escarpment (25–70 mm/kyr [*Vanacker et al.*, 2007]) and to basin-average rates that prevail in tropical Puerto Rico ($\sim$40 mm/kyr) [*Brown et al.*, 1995; *Riebe et al.*, 2003].

5.2. Potential Effects of Glaciation on Cosmogenic Nuclide Concentrations and Basins Morphology

5.2.1. Effects on Cosmogenic Nuclide Concentrations

[43] The quantification of the extent of former and recent glaciation, and storage of old moraine material in the river basins is important, as steady state nuclide concentration may not have been reached after deglaciation, and the incorporation of low-nuclide material could bias TCN-based denudation rates. The extent of bias on denudation rates depends on the amount of area covered by glaciers and moraine material per basin, the time that has passed since the cessation of glaciation, and the prevailing erosion rate [*Wittmann et al.*, 2007].

[44] The contribution of low-concentration material to the river by glaciers of the recent Lac Gris glaciation can be regarded as negligible, due to the very limited extent of the Lac Gris stage [see also *Taylor et al.*, 2009; Figure 3b]. However, moraine material from older glaciation stages (Figure 3b) with potentially low nuclide concentrations [*Wittmann et al.*, 2007] may be preferentially remobilized and admixed to material eroded from the hillslopes under normal, steady state erosion processes. This admixing would result in a "dilution" effect of basin-wide nuclide concentrations. However, given that the moraine material is being irradiated by cosmic rays while exposed on valleys for a minimum exposure time of >11 kyr, we consider the moraine material (having a much lower density than bedrock) to be in cosmogenic nuclide steady state within the post-glacial time period.

[45] The re-establishment of steady state ^{10}Be-concentrations in bedrock surfaces since melting of >100 kyr old glaciers is ascertained by modeling (see Figure 5). However, it is questionable whether enough time has passed since retreat of the LGM and 11.6 kyr BP glaciation stages to restore steady state conditions in the slowly eroding Rwenzori Mountains. In settings with rapid erosion rates, a fast approach to steady state after de-glaciation can be safely assumed [*Wittmann et al.*, 2007]. To this end, we explore the approach of steady state after surface zeroing by adopting the numerical model of *von Blanckenburg* [2005] (see Section 3.3), modified to the special setting of the Rwenzoris. Figure 5 shows that the modeled or "real" denudation rate does not reach the prescribed input steady state denudation of $\sim$50 mm/kyr (blue line, case 1 in Figure 5), but overestimates denudation by $\sim$50% at time zero (today), by yielding a rate of $\sim$80 mm/kyr (stippled line, case 2 in Figure 5). For this scenario, however, we assumed complete zeroing of surface nuclide concentrations; thus, this scenario is seen as a "worst case," in which the maximum overestimation in denudation is approached. In reality, some basins (e.g., 316 and 359) were affected only to a small extent by LGM glaciation (Table 2, Section 2.3), and these basins erode today at rates that are below the prescribed steady state denudation of 50 mm/kyr. However, for the three high-relief basins 373, 388, and 491, the glaciated portions of the basin area during the LGM and during the Omirubaho stage were far higher (Table 2, Section 2.3). If we assume that the measured denudation rates from these basins (e.g., 74, 108, and 131 mm/kyr, respectively, see Table 1) are biased by a maximum overestimation of 50%, these basins would erode at minimum rates between $\sim$50 and 100 mm/kyr. These denudation rates would again be in the same range as the average for all northern basins. To summarize, we acknowledge that the three high-relief basins 373, 388, and 491 may be biased toward higher denudation rates, and a worst-case scenario estimates this overestimation to be 50%.

5.2.2. Effects on Basin Morphology

[46] Evidence for glacial forcing of basin morphology in high-altitude parts of the Rwenzori Mountains is provided by several observations. First and most importantly, our river profile analysis (Figure 7) shows that alternating steep and flat reaches, along with a tendency for a convex shape, occur in close relation to glacial ELAs, altogether implying a glacial erosional overprint (compare *Whipple et al.* [1999] and *Brocklehurst and Whipple* [2006]). In addition, the most prominent knickpoints of river profiles 373, 491, and 388 are associated with ELA levels. Second, glacial striae are locally still visible on bedrock surfaces exposed at the valley sides. Third, field observations provide evidence that debris of post-glacial slope failure activity at oversteepened cliffs in high-altitude regions is only weakly coupled to the modern drainage system. Overall, the above assessment indicates that in high-altitude parts of the river basins, post-glacial fluvial erosion has not yet significantly affected basin morphology. On the other hand, in most basins' lower reaches, there is evidence for fluvial erosion having mainly shaped basin morphology. For example, river profiles change to more or less clear concave shapes in basins 399, 294, 295, 337, and 538 and hence mark abiding ice-free geomorphology.

[47] To summarize, there are very few indications that the glacial morphology of high-altitude regions has been

Table 3. Basin Geology: Proportions of Basement Lithology of Each Basin

Basement Rock Type	Northern Mountainous Catchments							Southern Mountainous Catchments							Platform Catchments			Rift Shoulder Catchment
	294	295	300	311	316	321	337	359	373	375	388	398	399	491	9	24	28	538
Amphibolite	0	0	0	0	0	0	0	28.9	31.7	0	0	0	0	0	0	0.1	0	0
Gneiss	100	77.8	100	88.8	93.2	83.8	100	43.5	44.3	35.3	79.2	63.6	50.6	60.2	79.5	52.0	24.3	61.2
undifferentiated schists with quartzite bands (including Bugoye Schist group)	0	22.2	0	11.1	0	10.3	0	25.8	19.2	57.5	20.8	36.4	43.4	39.8	1.3	45.3	68.9	0
Granite	0	0	0	0	0	0	0	0	0	0	0	0	0	0	0	1.1	0	0
Sediments (Miocene to recent)	0	0	0	0	6.8	5.9	0	1.8	4.8	7.2	0	0	6.0	0	0	0.54	0	38
Volcanics	0	0	0	0	0	0	0	0	0	0	0	0	0	0	19.2	1	6.8	0.8

changed significantly by fluvial erosional processes and/or mass wasting. Clearly, inter- and post-glacial fluvial erosional processes were not yet able to equilibrate glacial morphology, as glacial landforms are often preserved. However, in areas located mainly below ELA levels, we suggest that knickpoints are, in most cases, probably related to repeated pulses of rock uplift.

5.3. Climate and Vegetation

[48] In the Rwenzori Mountains, the percentage of unvegetated bedrock area correlates with denudation rate (see Tables 1 and 2). We infer here that this correlation is a climatic-driven feedback, because bare bedrock areas are only present in areas above 4500 m a.s.l., where temperatures around zero degrees prevail, and frost shattering can promote higher physical erosion. On the other hand, the permanent cloud immersion of the mountains directly causes a decrease of diurnal temperature fluctuations and hence reduces frost-shattering processes. In lower-altitude regions, the presence of vegetation then enhances this temperature-regulated reduction of physical erosion. Thus, in these vegetated areas, we suggest that the rapid physical erosion that normally occurs in such high relief settings is considerably reduced by the prevailing tropical montane cloud forest conditions. Vegetation cover reduces soil erosion by intercepting raindrops, enhancing infiltration, transpiring soil water, and increasing surface roughness [Castillo et al., 1997; Gyssels et al., 2005; Lancaster and Baas, 1998; Rogers and Schumm, 1991]. The strong seasonal fluctuations in precipitation and water budget are buffered in vegetated areas of the Rwenzori Mountains and the occurrence of less extreme runoff events in high-altitude zones is facilitated by high, but constant runoff [Foster, 2001]. Overall, we suggest that the combination of horizontal (cloud-filtered) precipitation from permanent cloud immersion, mild climate with reduced diurnal temperature fluctuations, and non-seasonal dense vegetation cover dampening raindrop impacts limits non-vegetated bedrock areas to peaks and ridges, which might lead to fewer mass wasting events and overall lower denudation rates.

5.4. Bedrock Lithology and Erodibility

[49] If rock strength exerts a primary control on erosion, correlation patterns between lithology, denudation rate, local hillslope gradients, and channel steepness with denudation rate should exist [Schmidt and Montgomery, 1995; Montgomery, 2001]. However, we find no direct correlation between lithology and denudation rate from the low-resolution lithological map that is available for the region (Figure 3a), nor do we observe a direct correlation between hillslope gradients and lithology. The catchments with overall highest slopes of >21° (see Table 2) occur in different areas of the Rwenzori block independent of the presence of a certain prevailing bedrock lithology (Table 3 and Figure 3a). Also, similar hillslope gradients for all northern catchments (20.4°, mean denudation rate ~52 mm/kyr) and all southern catchments (19.7°, mean denudation rate ~72 mm/kyr) show that erodibility contrasts due to differences in lithologic composition have no systematic effect on denudation rates. Only in the case of the non quartz-bearing amphibolite can we tie its resistant lithology, presumably having the lowest erodibility, to higher mean slope gradients (see Figure 3a). Regarding values of channel steepness k_{sn} and lithology, we observe local changes in all k_{sn} at lithological boundaries, but we cannot attribute typical k_{sn} values to certain lithologies, as all k_{sn} values are present in all lithologies (see Figure 3a).

5.5. Topography, Basin Average Slope, and Channel Steepness

[50] The positive linear correlation between denudation rate and mean elevation (Figure 8c) with high relief catchments eroding much faster than low relief basins is characteristic for areas where there are gradients in uplift [e.g., Binnie et al., 2007; Montgomery, 2001]. Noteworthy is that our data reveals somewhat lower basin average slopes compared to other high relief settings (e.g., Alps, Himalayas [see Wittmann et al., 2007; Ouimet et al., 2009]). As the evolution of gentler slopes is attributed to regolith-covered hillslopes and accordingly, the evolution of steeper cliffs to bare rock areas [e.g., Pelletier and Rasmussen, 2009], this fact is not surprising regarding the soil-covered nature of the setting. With a maximum hillslope gradient of 24° approached by some high-altitude basins, we conclude that, in the Rwenzori Mountains, hillslopes are far from being threatened by mass wasting processes, and hillslope gradients are not at threshold conditions. These two observations are concurrent with our overall low TCN-derived denudation rates. We find that 1) hillslope failure occurs only rarely in the vegetated zones of the mountainous Rwenzori basins, and relatively low average hillslope gradients correlate linearly with denudation rates for the majority of basins (see Figure 8b). Exceptions

are basins 373, 491, and 388, which fall above a linear trend and show higher (potentially over-estimated, see Section 5.2.1) denudation rates. 2) Similarly, channel steepness index k_{sn} and hillslope gradients correlate reasonably well in the Rwenzoris (see Figure 8e), but this correlation may be biased by glacial imprinting, and 3) most of our basins do not show negative skewness of hillslope distributions, an indication for hillslope failure. On the contrary, we find mostly positive skewness, indicating that depositional processes are more important than erosional processes [*Wolinsky and Pratson*, 2005]. 4) Rockfalls occur at a moderate extent in the non-vegetated high-altitude crest regions. The limited number of rockfalls is also indicated by uniform grain size-specific cosmogenic nuclide concentrations. If rockfall events were to contribute a large proportion of the erosion relative to steady state bedrock to soil conversion, lower nuclide concentrations would be found in the coarser grain size fraction, as rockfall material is to a large extent produced below the mean cosmogenic nuclide attenuation depth.

[51] To summarize, upper, high-altitude parts of the Rwenzori Mountains appear to be strongly affected by glacial imprinting. Here, mass wasting processes might contribute to basin-wide erosion at a larger extent. This might especially be the case in basins 373, 491, and 388, where transient, or unequilibrated convex river profiles reach the mid-sections. In other basins below ELA levels, fluvial processes like river incision have gained more influence, with stochastic erosion processes like mass wasting probably only playing a minor role. Here, we suggest that river incision, as indicated by channel steepness indices, is trying to balance uplift to smooth out knickpoints along the rivers.

6. The Current State of Uplift and Erosion in the Rwenzori Mountains

[52] It is beyond the scope of this paper to derive an evolutionary model for the Rwenzori Mountains, but on the basis of already published assessments, and our millennial-scale erosion data, we discuss in the following whether erosion and uplift are balanced in this setting. To begin with, a direct relation between the exhumation of the Rwenzori Mountains and the activity of the rift system is inferred from geodynamic modeling [*Wallner and Schmeling*, 2010]. Also, from low-temperature thermochronology, apatite fission track, and apatite U-Th-Sm/He analysis, average uplift rates of >200 mm/kyr were derived for the last 20 Myr [*Bauer et al.*, 2010]. A syn-rift sediment record of a graben area NE of the Rwenzori range provides long-term sedimentation rates that increased from 20 to 40 mm/kyr to 100 mm/kyr [*Pickford et al.*, 1993; *Roller et al.*, 2010], indicating that graben subsidence and footwall uplift accelerated at around 2 Myr.

[53] Ongoing relative plate motion [*Stamps et al.*, 2008; *Calais et al.*, 2006], and the occurrence of a flexural uplift pulse of the rift shoulder at 14–12 kyr BP (see Section 2.1) support the hypothesis that the Rwenzori block is in a long-term state of active tectonics. Our analysis of landscape parameters and [10]Be nuclide concentrations in river sand tentatively supports this hypothesis, by showing that: (i) Some of the river long profiles show geometries inherited from glaciations (stepped, concave up), especially in upper parts of

the basins, and thus are far from having reached equilibrium. (ii) The channel steepness values indicate that river incision locally acts at high rates trying to balance uplift and to smooth knickpoints along the rivers. Again, we find that this effect is concentrated in lower-altitude areas where the morphology has been shaped by post-glacial sculpting. (iii) Our TCN-derived denudation rates are in the range of long-term, syn-rift record-derived sedimentation rates (from direct vicinity of the Rwenzori Mountains [see *Roller et al.*, 2010]), suggesting that our rates represent a longer-term signal. (iv) In addition, denudation rates of the Rwenzori Mountains are much lower than those rates of most other tectonically active settings, and erode more in the range of tropical, tectonically non-active settings.

7. Conclusions

[54] The highest non-volcanic topographic elevation of the African continent, the Rwenzori Mountain fault block situated within the East African Rift, erodes at cosmogenic nuclide-derived denudation rates between 7.8 and 131 mm/kyr during the last 6–100 kyr. In situ [10]Be-derived denundation rates of the high relief mountainous basins amount to 59.9 ± 31.2 mm/kyr (1σ SD), and those of the flat topography rift shoulder and surrounding lowland catchments erode at lower rates of 11.6 ± 5.4 mm/kyr (1σ SD). We provide the following explanations for these unexpected low denudation rates in a humid and high-relief tropical setting:

[55] (1) Climatic effects. Due to the high topography, a tropical montane cloud forest climate exists, with vegetation covering >90% of catchment area. Faster physical erosion that would normally occur in such high relief settings is reduced by these specific climatic conditions, as strong seasonal fluctuations in precipitation and the soils' water budget are effectively buffered. The lack of dry seasons promotes vegetation growth up to the highest mountain peaks, resulting in low frost shattering activity and limited bare rock areas, and the lack of pronounced melting seasons prevents immediate sediment mobilization and export.

[56] (2) Paraglacial and glacial effects. The high abrasion energy associated with glaciations and the ability to produce high local relief quickly diminished since LGM termination at ~11.6 kyr. Since then, post-glacial fluvial erosion has commenced to sculpt the landscape. However, we find evidence for a nonsteady state, or transient landscape, as post-glacial fluvial erosional processes have apparently not yet been able to equilibrate glacial morphologies.

[57] (3) Geological effects. Apart from its predominantly high-grade gneissic lithology with low erodibility, the seismicity pattern of the region indicates that deformation and earthquake-induced fault movement is limited to major shear zones around the fault block. Thus, the potential of seismicity to trigger hillslope failure and degrees of fracturing are low for the internal regions of the fault block.

[58] (4) Changes in erosion and uplift over time. Long-term Neogene sedimentation rates in the immediate vicinity of the Rwenzori Mountains are consistent with our millennial-scale TCN-based denudation rates. From our river profile analysis, we suggest that uplift in the Rwenzoris is ongoing, although we cannot quantify uplift velocity.

[59] To conclude, we suggest that highly erosion-resistant rocks and low degrees of internal fracturing interact with the

specific climatic conditions of the Rwenzori Mountains, thereby causing denudation rates in this extensional setting in the humid tropics of East Africa to be overall relatively low for this tectonically active area. This outcome highlights the need for substantial research in tropical, tectonically active areas, where the key for unraveling climatic versus tectonic effects on erosion might be found.

References

Allison, R. J. (1994), Slopes and slope processes, *Prog. Phys. Geogr.*, *18*(3), 425–435, doi:10.1177/030913339401800309.

Augustinus, P. C. (1995), Glacial valley cross-profile development: The influence of in situ rock stress and rock mass strength, with examples from the Southern Alps, New Zealand, *Geomorphology*, *14*, 87–97, doi:10.1016/0169-555X(95)00050-X.

Balco, G., J. O. Stone, N. A. Lifton, and T. J. Dunai (2008), A complete and easily accessible means of calculating surface exposure ages or erosion rates from Be-10 and Al-26 measurements, *Quat. Geochronol.*, *3*(3), 174–195, doi:10.1016/j.quageo.2007.12.001.

Bauer, F., U. Glasmacher, U. Ring, A. Schumann, and B. Nagudi (2010), Thermal and exhumation history of the central Rwenzori Mountains, Western Rift of the East African Rift System, Uganda, *Int. J. Earth Sci.*, *99*, 1575–1597, doi:10.1007/s00531-010-0549-7.

Berlin, M. M., and R. S. Anderson (2009), Steepened channels upstream of knickpoints: Controls on relict landscape response, *J. Geophys. Res.*, *114*, F03018, doi:10.1029/2008JF001148.

Binnie S. A., W. M. Phillips, M. A. Summerfield, and L. K. Fifield (2007), Tectonic uplift, threshold hillslopes, and denudation rates in a developing mountain range, *Geology*, *35*, 743–746, doi:10.1130/G23641A.1.

Bishop, W. W., and A. F. Trendall (1966), Erosion surfaces, tectonics and volcanic activity in Uganda, *Q. J. Geol. Soc. London*, *122*, 385–420, doi:10.1144/gsjgs.122.1.0385.

Brocklehurst, S. H., and K. X. Whipple (2006), Assessing the relative efficiency of fluvial and glacial erosion through simulation of fluvial landscapes, *Geomorphology*, *75*, 283–299, doi:10.1016/j.geomorph.2005.07.028.

Brown, E. T., R. F. Stallard, M. C. Laren, G. M. Raisbeck, and F. Yiou (1995), Denudation rates determined from the accumulation of in-situ produced [10]Be in the Luquillo experimental forest, Puerto Rico, *Earth Planet. Sci. Lett.*, *129*, 193–202.

Calais, E., C. Hartnady, C. Ebinger, and J. M. Nocquet (2006), Kinematics of the East African Rift from GPS and earthquake slip vector data, *Geol. Soc. Spec. Publ.*, *259*, 9–22, doi:10.1144/GSL.SP.2006.259.01.03.

Castillo, V. M., M. Martinez-Mena, and J. Albaladejo (1997), Runoff and soil loss response to vegetation removal in a semiarid environment, *Soil Sci. Soc. Am. J.*, *61*, 1116–1121, doi:10.2136/sssaj1997.03615995006100040018x.

Chmeleff, J., F. von Blanckenburg, K. Kossert, and D. Jakob (2010), Deter-mination of the [10]Be half-life by multicollector ICP-MS and liquid scintil-lation counting, *Nucl. Instrum. Methods Phys. Res., Sect. B*, *268*, 192–199, doi:10.1016/j.nimb.2009.09.012.

Chorowicz, J. (2005), The East African rift system, *J. Afr. Earth Sci.*, *43*, 379–410, doi:10.1016/j.jafrearsci.2005.07.019.

Coetzee, J. A., and E. M. van Zinderen Bakker (1989), Palaeoclimatology of East Africa during the Last glacial maximum: A review of changing theories, in *Quaternary and Environmental Research on East African Mountains*, edited by W. C. Mahaney, pp. 189–198, A. A. Balkema, Rotterdam, Netherlands.

Cyr, A. J., D. E. Granger, V. Olivetti, and P. Molin (2010), Quantifying rock uplift rates using channel steepness and cosmogenic nuclide-

determined erosion rates: Examples from northern and southern Italy, *Lithosphere*, *2*, 188–198.

Dunai, T. J. (2000), Scaling factors for production rates of in situ produced cosmogenic nuclides: A critical reevaluation, *Earth Planet. Sci. Lett.*, *176*, 157–169, doi:10.1016/S0012-821X(99)00310-6.

Ebinger, C. J. (1989), Tectonic development of the western branch of the East African rift system, *Geol. Soc. Am. Bull.*, *101*, 885–903, doi:10.1130/0016-7606(1989)101<0885:TDOTWB>2.3.CO;2.

Food and Agriculture Organization of the United Nations (2000), Global Forest Resources Assessment, *Main Rep. 140*, Rome.

Foster, P. (2001), The potential negative impacts of global climate change on tropical montane cloud forests, *Earth Sci. Rev.*, *55*, 73–106.

Granger, D. E., J. W. Kirchner, and R. Finkel (1996), Spatially averaged long-term erosion rates measured from in situ-produced cosmogenic nuclides in alluvial sediment, *J. Geol.*, *104*(3), 249–257, doi:10.1086/629823.

Gyssels, G., J. Poesen, E. Bochet, and Y. Li (2005), Impact of plant roots on the resistance of soils to erosion by water: a review, *Prog. Phys. Geogr.*, *29*(2), 189–217.

Hack, R., D. Price, and N. Rengers (2003), A new approach to rock slope stability–a probability classification (SSPC), *Bull. Eng. Geol. Environ.*, *62*, 167–184.

Hamilton, L. S. (1995), Mountain cloud forest conservation and research: A synopsis, *Mt. Res. Dev.*, *15*(3), 259–266, doi:10.2307/3673933.

Hastenrath, S. (2009), Past glaciation in the tropics, *Quat. Sci. Rev.*, *28*(9–10), 790–798, doi:10.1016/j.quascirev.2008.12.004.

Hewawasam, T., F. von Blanckenburg, M. Schaller, and P. Kubik (2003), Increase of human over natural erosion rates in tropical highlands con-strained by cosmogenic nuclides, *Geology*, *31*(7), 597–600, doi:10.1130/0091-7613(2003)031<0597:IOHONE>2.0.CO;2.

Insel, N., T. A. Ehlers, M. Schaller, J. B. Barnes, S. Tawackoli, and C. J. Poulsen (2010), Spatial and temporal variability in denudation across the Bolivian Andes from multiple geochronometers, *Geomorphology*, *122*, 65–77, doi:10.1016/j.geomorph.2010.05.014.

Johnson, T. C., C. A. Scholz, M. R. Talbot, K. Kelts, G. N. Ricketts, K. Beuning, I. Ssemmanda, and J. W. McGill (1996), Late Pleistocene desiccation of Lake Victoria and rapid evolution of cichlid fishes, *Science*, *273*, 1091–1093, doi:10.1126/science.273.5278.1091.

Johnson, W. (1972), *Impact Strength of Materials*, 361 pp., Edward Arnold, New York.

Kappelle, M. (2004), Tropical montane forests, in *Encyclopedia of Forest Sciences*, edited by J. Burley, pp. 1782–1792, Elsevier, Oxford, U. K., doi:10.1016/B0-12-145160-7/00175-7.

Kaser, G., and H. A. Osmaston (2002), *Tropical Glaciers* (*With Map of Glaciers and Glaciations of the Rwenzori Mountains, Uganda*), 207 pp., Cambridge Univ. Press, Cambridge, U. K.

Kiage, L. M., and K. Liu (2006), Late Quaternary paleoenvironmental changes in East Africa: A review of multiproxy evidence from palynology, lake sediments, and associated rocks, *Prog. Phys. Geogr.*, *30*(5), 633–658, doi:10.1177/0309133306071146.

Koehn, D., K. Aanyu, S. Haines, and T. Sachau (2007), Rift nucleation, rift propagation and the creation of basement micro-plates within active rifts, *Tectonophysics*, *458*(1–4), 105–116.

Korschinek, G., et al. (2010), A new value for the half-life of [10]Be by Heavy-Ion Elastic Recoil Detection and liquid scintillation counting, *Nucl. Instrum. Methods Phys. Res., Sect. B*, *268*, 187–191, doi:10.1016/j.nimb.2009.09.020.

Korup, O., and F. Schlunegger (2009), Rock-type control on erosion-induced uplift, eastern Swiss Alps, *Earth Planet. Sci. Lett.*, *278*, 278–285, doi:10.1016/j.epsl.2008.12.012.

Kubik, P. W., and M. Christl (2010), [10]Be and [26]Al measurements at the Zurich 6 MV Tandem AMS facility, *Nucl. Instrum. Methods Phys. Res., Sect. B*, *268*, 880–883, doi:10.1016/j.nimb.2009.10.054.

Kubik, P. W., M. Christl, and V. Alfimov (2009), New primary [10]Be stan-dard and $t_{1/2}$ for AMS at ETH: Recalibration of the in-house [10]Be stan-dards, annual report, 12 pp., ETH Zurich, Zurich, Netherlands.

Kühni, A., and O. A. Pfiffner (2001), The relief of the Swiss Alps and adja-cent areas and its relation to lithology and structure: Topographic analysis from a 250-m DEM, *Geomorphology*, *41*, 285–307, doi:10.1016/S0169-555X(01)00060-5.

Lancaster, N., and A. Baas (1998), Influence of vegetation cover on sand transport by wind: Field studies at Owens Lake, California, *Earth Surf. Processes Landforms*, *23*, 69–82, doi:10.1002/(SICI)1096-9837(199801)23:1<69::AID-ESP823>3.0.CO;2-G.

Lindenfeld, M., G. Rumpker, H. Schmeling, and H. Wallner (2010), Seismicity Patterns and Magmatic Processes in the Rwenzori Region, East-African Rift, Abstract T31C-2192 presented at 2010 Fall Meeting, AGU, San Francisco, Calif., 13–17 Dec.

Livingstone, D. A. (1967), Postglacial vegetation of the Rwenzori Mountains in equatorial Africa, *Ecol. Monogr.*, 37, 25–52, doi:10.2307/1948481.

Maasha, N. (1975), The seismicity of the Ruwenzori region in Uganda, *J. Geophys. Res.*, 80, 1485–1496, doi:10.1029/JB080i011p01485.

Maden, C., P. A. F. Anastasi, A. Dougans, S. P. H. T. Freeman, R. Kitchen, G. Klody, C. Schnabel, M. Sundquist, K. Vanner, and S. Xu (2007), SUERC AMS ion detection, *Nucl. Instrum. Methods Phys. Res., Sect. B*, 259, 131–139, doi:10.1016/j.nimb.2007.01.151.

Marchant, R., and H. Hooghiemstra (2004), Rapid environmental change in African and South American tropics around 4000 years before present: A review, *Earth Sci. Rev.*, 66, 217–260, doi:10.1016/j.earscirev.2004.01.003.

Matmon, A., P. R. Bierman, J. Larsen, S. Southworth, M. Pavich, R. Finkel, and M. Caffee (2003), Erosion of an ancient mountain range, the Great Smoky Mountains, North Carolina and Tennessee, *Am. J. Sci.*, 303, 972–973, doi:10.2475/ajs.303.10.972.

Montgomery, D. R. (2001), Slope distribution, threshold hillslopes, and steady-state topography, *Am. J. Sci.*, 301, 432–454, doi:10.2475/ajs.301.4-5.432.

Nishiizumi, K., M. Imamura, M. W. Caffee, J. R. Southon, R. C. Finkel, and J. Aninch (2007), Absolute calibration of ^{10}Be AMS standards, *Nucl. Instrum. Methods Phys. Res., Sect. B*, 258(2), 403–413, doi:10.1016/j.nimb.2007.01.297.

Norton, K. P., and V. Vanacker (2009), Effects of terrain smoothing on topographic shielding correction factors for cosmogenic nuclide-derived estimates of basin-averaged denudation rates, *Earth Surf. Processes Landforms*, 34, 145–154, doi:10.1002/esp.1700.

Norton, K. P., F. von Blanckenburg, and P. W. Kubik (2010), Cosmogenic nuclide-derived rates of diffusive and episodic erosion in the glacially sculpted upper Rhone Valley, Swiss Alps, *Earth Surf. Processes Landforms*, 35(6), 651–662.

Ollier, C. D. (1959), A two-cycle theory of tropical pedology, *J. Soil Sci.*, 10(2), 137–148, doi:10.1111/j.1365-2389.1959.tb02338.x.

Osmaston, H. (1989), Glaciers, glaciation and equilibrium line altitudes on the Rwenzori, in *Quaternary and Environmental Research on East African Mountains*, edited by W. C. Mahaney, pp. 31–104, A. A. Balkema, Rotterdam, Netherlands.

Osmaston, H., and S. P. Harrison (2005), The Late Quaternary glaciation of Africa: A regional synthesis, *Quat. Int.*, 138–139, 32–54, doi:10.1016/j.quaint.2005.02.005.

Osmaston, H., and G. Kaser (2001), *Rwenzori Mountains National Park, Uganda and Parc National des Virungas, Democratic Republic of Congo Glaciers and Glaciations*, WWF, Washington, D. C.

Ouimet, W. B., K. X. Whipple, and D. E. Granger (2009), Beyond threshold hillslopes: Channel adjustment to base-level fall in tectonically active mountain ranges, *Geology*, 37, 579–582, doi:10.1130/G30013A.1.

Palumbo, L., R. Hetzel, M. Tao, and X. Li (2010), Topographic and lithologic control on catchment-wide denudation rates derived from cosmogenic ^{10}Be in two mountain ranges at the margin of NE Tibet, *Geomorphology*, 117, 130–142, doi:10.1016/j.geomorph.2009.11.019.

Pelletier, J. D., and C. Rasmussen (2009), Quantifying the climatic and tectonic controls on hillslope steepness and erosion rate, *Lithosphere*, 1, 73–80, doi:10.1130/L3.1.

Phillips, J. D., and J. D. Lutz (2008), Profile convexities in bedrock and alluvial streams, *Geomorphology*, 102, 554–566, doi:10.1016/j.geomorph.2008.05.042.

Pickford, M., B. Senut, and D. Hadoto (1993), *Geology and Palaeobiology of the Albertine Rift Valley, Uganda–Zaire*, Cent. Int. Form. Echanges Geol., Paris.

Portenga, E. W., and P. Bierman (2011), Understanding Earth's eroding surface with ^{10}Be, *GSA Today*, 21(8), 4–10, doi:10.1130/G111A.1.

Riebe, C. S., J. W. Kirchner, D. E. Granger, and R. C. Finkel (2000), Erosional equilibrium and disequilibrium in the Sierra Nevada, inferred from cosmogenic Al-26 and Be-10 in alluvial sediment, *Geology*, 28(9), 803–806, doi:10.1130/0091-7613(2000)28<803:EEADIT>2.0.CO;2.

Riebe, C. S., J. W. Kirchner, and R. C. Finkel (2003), Long-term rates of chemical weathering and physical erosion from cosmogenic nuclides and geochemical mass balance, *Geochim. Cosmochim. Acta*, 67(22), 4411–4427, doi:10.1016/S0016-7037(03)00382-X.

Ring, U. (2008), Extreme uplift of the Rwenzori Mountains in the East African Rift, Uganda: Structural framework and possible role of glaciations, *Tectonics*, 27, TC4018, doi:10.1029/2007TC002176.

Roebber, P. J., S. L. Bruening, D. M. Schultz, and J. V. Cortinas Jr. (2003), Improving snowfall forecasting by diagnosing snow density, *Weather Forecast.*, 18, 264–287.

Rogers, R. D., and S. A. Schumm (1991), The effect of sparse vegetative cover on erosion and sediment yield, *J. Hydrol.*, 123, 19–24, doi:10.1016/0022-1694(91)90065-P.

Roller, S., J. Hornung, M. Hinderer, and I. Ssemmanda (2010), Middle Miocene to Pleistocene sedimentary record of rift evolution in the southern Albert Rift (Uganda), *Int. J. Earth Sci.*, 7, 1643–1661, doi:10.1007/s00531-010-0560-z.

Safran, E. B., P. Bierman, R. Aalto, T. Dunne, K. X. Whipple, and M. Caffee (2005), Erosion rates driven by channel network incision in the Bolivian Andes, *Earth Surf. Processes Landforms*, 30, 1007–1024, doi:10.1002/esp.1259.

Schaller, M., F. von Blanckenburg, A. Veldkamp, L. A. Tebbens, N. Hovius, and P. W. Kubik (2002), A 30,000 yr record of erosion rates from cosmogenic ^{10}Be in Middle European river terraces, *Earth Planet. Sci. Lett.*, 204, 307–320, doi:10.1016/S0012-821X(02)00951-2.

Schildgen, T., D. Cosentino, B. Bookhagen, S. Niedermann, C. Yildirim, H. Echtler, H. Wittmann, and M. R. Strecker (2012), Multi-phased uplift of the southern margin of the Central Anatolian plateau, Turkey: A record of tectonic and upper mantle processes, *Earth Planet. Sci. Lett.*, 317–318, 85–95, doi:10.1016/j.epsl.2011.12.003.

Schmidt, K. M., and D. R. Montgomery (1995), Limits to relief, *Science*, 270, 617–620, doi:10.1126/science.270.5236.617.

Stadtmüller, T. (1987), *Cloud Forests in the Humid Tropics*, 82 pp., United Nations Univ. Press, Turrialba, Costa Rica.

Stamps, D. S., E. Calais, E. Saria, C. Hartnady, J.-M. Nocquet, C. Ebinger, and R. M. Fernandes (2008), A kinematic for the East African Rift, *Geophys. Res. Lett.*, 35, L05304, doi:10.1029/2007GL032781.

Taylor, R. G., and K. W. F. Howard (1998), Post-Paleozoic evolution of weathered landsurfaces in Uganda by tectonically controlled deep weathering and stripping, *Geomorphology*, 25, 173–192, doi:10.1016/S0169-555X(98)00040-3.

Taylor, R. G., and K. W. F. Howard (1999), Lithological evidence for the evolution of weathered mantles in Uganda by tectonically controlled cycles of deep weathering and stripping, *Catena*, 35, 65–94, doi:10.1016/S0341-8162(98)00118-0.

Taylor, R. G., L. Mileham, C. Tindimugaya, A. Majugu, A. Muwanga, and B. Nakileza (2006), Recent glacial recession in the Rwenzori Mountains of East Africa due to rising air temperature, *Geophys. Res. Lett.*, 33, L10402, doi:10.1029/2006GL025962.

Taylor, R. G., N. L. Rose, A. W. Mackay, V. Panizzo, L. Mileham, I. Ssemmanda, C. Tindimugaya, B. Nakileza, A. Muwanga, and J. Hau (2007), Climate Change and the Aquatic Ecosystem of the Rwenzori Mountains, Uganda, *Res. Rep. 113*, Environ. Change Res. Cent., Univ. College, London.

Taylor, R. G., L. Mileham, C. Tindimugaya, and L. Mwebembezi (2009), Recent glacial recession and its impact on alpine riverflow in the Rwenzori Mountains of Uganda, *J. Afr. Earth Sci.*, 55, 205–213, doi:10.1016/j.jafrearsci.2009.04.008.

Temple, P. H. (1968), Further observations on the glaciers of the Ruwenzori, *Geogr. Ann., Ser. A*, 50, 136–150.

Vanacker, V., F. von Blanckenburg, T. Hewawasam, and P. W. Kubik (2007), Constraining landscape development of the Sri Lankan escarpment with cosmogenic nuclides in river sediment, *Earth Planet. Sci. Lett.*, 253, 402–414, doi:10.1016/j.epsl.2006.11.003.

Vance, D., M. Bickle, S. Ivy-Ochs, and P. Kubik (2003), Erosion and exhumation in the Himalaya from cosmogenic isotope inventories of river sediments, *Earth Planet. Sci. Lett.*, 206, 273–288.

von Blanckenburg, F. (2005), The control mechanisms of erosion and weathering at basin scale from cosmogenic nuclides in river sediment, *Earth Planet. Sci. Lett.*, 237, 462–479, doi:10.1016/j.epsl.2005.06.030.

von Blanckenburg, F., N. Belshaw, and R. K. O'Nions (1996), Separation of Be-9 and cosmogenic Be-10 from environmental materials and SIMS isotope dilution analysis, *Chem. Geol.*, 129, 93–99, doi:10.1016/0009-2541(95)00157-3.

Wallner, H., and H. Schmeling (2010), Rift induced delamination of mantle lithosphere and crustal uplift: A new mechanism for explaining Rwenzori Mountains' extreme elevation? *Int. J. Earth Sci.*, 99, 1511–1524, doi:10.1007/s00531-010-0521-6.

Whipple, K. X., E. Kirby, and S. H. Brocklehurst (1999), Geomorphic limits to climate-induced increases in topographic relief, *Nature*, 401, 39–43, doi:10.1038/43375.

Wittmann, H., F. von Blanckenburg, T. Kruesmann, K. P. Norton, and P. W. Kubik (2007), Relation between rock uplift and denudation from cosmogenic nuclides in river sediment in the Central Alps of Switzerland, *J. Geophys. Res.*, 112, F04010, doi:10.1029/2006JF000729.

Wittmann, H., F. von Blanckenburg, J. L. Guyot, L. Maurice, and P. W. Kubik (2009), From source to sink: Preserving the cosmogenic 10Be-derived denudation rate signal of the Bolivian Andes in sediment of the Beni and Mamoré foreland basins, *Earth Planet. Sci. Lett.*, 288, 463–474, doi:10.1016/j.epsl.2009.10.008.

Wobus, C., A. Heimsath, K. Whipple, and K. Hodges (2005), Active out-of-sequence thrust faulting in the central Nepalese Himalaya, *Nature*, *434*(7036), 1008–1011, doi:10.1038/nature03499.

Wobus, C., K. X. Whipple, E. Kirby, N. Snyder, J. Johnson, K. Spyropolou, B. Crosby, and D. Sheehan (2006), Tectonics from topography: Procedures, promise, and pitfalls, *Geol. Soc. Am. Spec. Publ.*, *398*, 55–74.

Wolinsky, M., and L. F. Pratson (2005), Constraints on landscape evolution from slope histograms, *Geology*, *33*, 477–480.

Xu, S., A. B. Dougans, S. P. H. T. Freeman, C. Schnabel, and K. M. Wilcken (2010), Improved ^{10}Be and ^{26}Al-AMS with a 5 MV spectrometer, *Nucl. Instrum. Methods Phys. Res., Sect. B*, *268*, 736–738, doi:10.1016/j.nimb.2009.10.018.

Young, J. A. T., and S. Hastenrath (1987), Glaciers of Africa. Satellite image atlas of glaciers of the world, *U.S. Geol Surv. Prof. Pap.*, *1386*, 49–70.